Reactive-transport modeling of neodymium and its radiogenic isotope in deep-sea sediments: the roles of authigenesis, marine silicate weathering and reverse weathering

Jianghui Du[a], Brian A. Haley[b], Alan C. Mix[b], April Abbott[c], James McManus[d], Derek Vance[a]

[a]Institute of Geochemistry and Petrology, Department of Earth Sciences, ETH Zürich, Clausiusstrasse 25, 8092, Zürich, Switzerland

[b]College of Earth Ocean and Atmospheric Sciences, Oregon State University, 104 CEOAS Admin. Bldg., Corvallis, OR 97331, USA

[c]Department of Marine Science, Coastal Carolina University, 100 Chanticleer Drive E, Conway, SC 29526, USA

[d]Bigelow Laboratory for Ocean Sciences, 60 Bigelow Drive, East Boothbay, ME 04544, USA

Corresponding to: Jianghui Du (jianghui.du@erdw.ethz.ch)

Abstract

Dissolved Rare Earth Elements (REE) and radiogenic neodymium (Nd) isotope composition (ε_{Nd}) of seawater are widely used geochemical tools in studying marine processes, but their modern ocean budgets are poorly understood. Recent discoveries of large benthic fluxes of REE with unique ε_{Nd} signatures from marine sediments, particularly in the deep-sea, have led to a "bottom-up" hypothesis, which suggests that early diagenesis below the sediment-water interface (SWI) controls the ocean's REE and ε_{Nd} budgets. To investigate such sedimentary processes, we created a reactive-transport model for the biogeochemical cycling of Nd and ε_{Nd} in marine sediments. Here, we attempt to quantify the roles of authigenesis, marine silicate weathering and reverse weathering in the diagenetic cycling of Nd and ε_{Nd} at a deep-sea (3000 m) site on the Oregon margin.

Our model predicts that, at this site, Nd carried by Fe/Mn oxides into sediments eventually transforms to authigenic Nd-phosphate, during which ~9% of the incoming solid Nd flux is released as a dissolved benthic flux back to the overlying bottom water. We also find that the classic reversible scavenging formulation applied to Nd co-cycling with Fe/Mn oxides is inconsistent with the data. Rather, a co-precipitation formulation, assuming Nd is structurally incorporated into Fe/Mn oxides, successfully simulates the data. The model also shows that authigenesis alone cannot explain the pore water and authigenic ε_{Nd}, which are both more radiogenic than bottom water at this site. However, the weathering of volcanic silicates sourced from the local subduction zone can successfully explain ε_{Nd}. We suggest that, because reverse weathering by authigenic clay formation maintains the under-saturation of primary silicates in pore water, marine silicate weathering can proceed. The processes we model likely affect the sedimentary cycling of many other trace elements and isotopes, with much broader implications for the understanding of ocean biogeochemistry.

Keywords:

Reactive-transport model, Rare Earth Elements, Radiogenic neodymium isotope, Authigenesis, Marine silicate weathering, Reverse weathering

1. Introduction

The seawater Rare Earth Elements (REE) are widely used geochemical tools for tracing ocean processes, such as circulation and the particulate-dissolved interaction known as Boundary Exchange (Elderfield and Greaves, 1982; Lacan and Jeandel, 2005; Piepgras et al., 1979). Among the 14 REE, neodymium (Nd) has received the most attention because its radiogenic isotope composition, expressed as $\varepsilon_{Nd}=[(^{143}Nd/^{144}Nd)_{sample}/(^{143}Nd/^{144}Nd)_{CHUR}-1]\times10^4$ where CHUR is the Chondritic Uniform Reservoir, gives additional constraints on the oceanic cycles of the REE (Goldstein and Hemming, 2003).

The applications of marine REE proxies have been hampered by our limited understanding of their modern oceanic budgets. Studies of marine Nd cycle have long identified a "missing source" problem: the known riverine and atmospheric inputs are too small to balance the global budgets, and some ~90% of the required sources needed to maintain the ocean inventory appears to be "missing" (Arsouze et al., 2009; Bertram and Elderfield, 1993; Tachikawa et al., 2003; Goldstein and Jacobsen, 1988).

Recently, the discovery of large benthic fluxes from marine sediment, with ε_{Nd} values that also satisfy the isotope budget, provides a promising candidate for this "missing source", leading to the "bottom-up" hypothesis of the marine REE cycles (Abbott et al., 2015a; Du et al., 2020; Haley et al., 2017). In this hypothesis, the sedimentary flux is the dominant source of ocean REE, and seawater ε_{Nd} signatures are acquired at the sediment-water interface (SWI) rather than at the river/atmosphere-ocean interface. Anomalous behavior of ε_{Nd} at the SWI has been documented (Grenier et al., 2013; Lacan and Jeandel, 2005; Lambelet et al., 2018), suggesting that processes involved in Boundary Exchange are indeed critical to trace element and isotopic budgets. It is thus important to understand the mechanisms of early diagenesis within sediments that derive these benthic fluxes, and how these processes contribute to the broader concepts of Boundary Exchange (Jeandel, 2016).

If correct, the "bottom-up" hypothesis would significantly change our interpretations of marine REE proxies; for example, the use of ε_{Nd} to trace paleo-circulation (Abbott et al., 2022; Du et al., 2020, 2018). However, studies of pore water REE concentrations and ε_{Nd} are scarce and mostly observational, with the mechanisms regulating the flux obscured by the complexity of sedimentary processes.

Here we report a reactive-transport model of the early diagenesis of Nd and ε_{Nd} in marine sediments with the intent of establishing the "bottom-up" hypothesis in mechanistic and quantitative terms. We focus

on deep-sea sediments where the benthic flux is the largest yet measured, potentially dominating the global budget (Abbott et al., 2015b; Du et al., 2020). We also present a test application of the model to a deep-sea site on the Oregon Margin, to date the only region for which a comprehensive pore water dataset exists (Abbott et al., 2019, 2016, 2015b, 2015a). We test three processes hypothesized to be critical in the diagenetic Nd cycle: (1) authigenesis of Fe-Mn oxides and phosphates (Schijf and Byrne, 2021; Takahashi et al., 2015; Bi et al., 2021; Abbott et al., 2016); (2) weathering of lithogenic sediments, for example silicate minerals (Abbott et al., 2022; Blaser et al., 2019; Du et al., 2020; Jeandel and Oelkers, 2015; Lacan and Jeandel, 2005), and (3) reverse weathering through conversion of biogenic silica to authigenic clay (Aller, 2014; Mackin and Aller, 1984). These processes are likely important for the sedimentary cycle of many trace elements and isotopes (TEIs), and our general modelling approach as well as the specific results for this site thus have implications for the global budgets of these TEIs. Our model also helps illuminate how authigenic phases acquire ε_{Nd} diagenetically, thus providing key insights for the use of authigenic ε_{Nd} in paleoceanography.

2. Study region

Paired REE and ε_{Nd} measurements in pore water and sediment, as well as ancillary data needed by the model, have only been made by Abbott et al., (2019, 2016, 2015b, 2015a) at three sites on the Oregon margin, Northeast Pacific (Fig. 1). We choose to model site HH3000 at 3000 m water depth, because it has one of the highest benthic Nd fluxes yet measured (~30 pmol/cm^2/yr). The water column here has a uniform ε_{Nd} of –2.4 ε, but pore water ε_{Nd} (–1.8 ε) is more radiogenic, the first evidence that diagenetic processes can decouple bottom and pore water ε_{Nd}.

The site underlies oxic bottom water (~100 μM) and has a low organic carbon rain rate (200 μg/cm^2/yr) (Lyle et al., 1992). These conditions lead to a weakly reducing shallow sediment package, with dissolved Mn (~50 μM) higher than Fe (<10 μM) in pore water (Abbott et al., 2016). Sediments are composed mainly of terrigenous materials (~90 wt%) with moderate organic carbon (OC) (~1.8 wt%), significant biogenic opal (~6 wt%), but negligible carbonate (~0.05 wt%). The accumulation rate is ~13 cm/kyr (Abbott et al., 2016; Lyle et al., 1992). Terrigenous sediments are delivered by small coastal rivers that drain across the Oregon Coastal Range and Cascade Arc. The mineral assemblage consists of quartz, plagioclase, chlorite

and muscovite/illite, with minor clinopyroxene, amphibole and volcanic glass (Abbott et al., 2019), reflecting their sources in the igneous and low-grade metamorphic rocks of the continental arc (VanLaningham et al., 2008).

3. Diagenetic modelling

Ours is a classic 1D reactive-transport model describing the distributions of dissolved species in pore water and solid species in sediments (Boudreau, 1997). Physical transport includes molecular diffusion, burial and bio-irrigation for dissolved species, and bioturbation and burial for solid species. The model includes the classic sequence of organic matter decomposition, and uses the continuum formulation of the reactivity of organic matter. The model also includes secondary redox reactions, dissolution of biogenic opal, $CaCO_3$ and precipitation of FeS/FeS_2. We also model pH for speciation calculations. Complete model details are given in the Supplementary Methods; here we only present those that relate to Nd and ε_{Nd}.

We model ^{144}Nd and radiogenic ^{143}Nd as two separate tracers. The convention for reporting radiogenic ε_{Nd} is to remove the natural and instrumental stable isotope fractionation by normalizing the $^{143}Nd/^{144}Nd$ ratio to a fixed $^{146}Nd/^{144}Nd$ ratio of 0.7219. A model of ε_{Nd} thus has no need to consider stable isotope fractionation. Modeled Nd concentration is the sum of these two isotopes divided by the summed natural abundance (0.35971). Nd speciation for both isotopes is computed following Schijf and Byrne (2021), considering complexation with dissolved ligands CO_3^{2-}, HCO_3^-, Cl^-, SO_4^{2-} and $H_3SiO_4^-$. We do not consider organic ligands since they have not been characterized in sediment pore water.

3.1. Authigenic Fe/Mn oxides

To date, interaction of Nd with solid phases in ocean models has been formulated as *equilibrium* reversible scavenging (Siddall et al., 2008). Using MnO_2 as an example (same for FeOOH):

$$^{i}Nd_{MnO_2} = {}^{i}Nd_d \times K_{ads\text{-}MnO_2} \times MnO_2, \quad (1)$$

where

$^{i}Nd_d$ is the *total* dissolved Nd concentration (i=143 or 144);

$^{i}Nd_{MnO_2}$ is the adsorbed Nd concentrations;

$K_{ads\text{-}MnO_2}$ is the adsorption constant specific to MnO_2.

We also consider an alternative *kinetic* co-precipitation formulation:

$$R^iNd_{Mn\text{-}pre} = RMn_{oxi} \times D_{Nd/Mn} \times {}^iNd_d/Mn_d, \quad (2)$$

$$R^iNd_{Mn\text{-}dis} = RMnO_{2_{red}} \times {}^iNd_{MnO_2}/MnO_2, \quad (3)$$

where

$R^iNd_{Mn\text{-}pre}$ is the co-precipitation rate of Nd when dissolved Mn (Mn_d) is oxidized at a rate of RMn_{oxi};

$D_{Nd/Mn}$ is the partition coefficient controlling the enrichment of Nd relative to Mn in MnO_2;

$R^iNd_{Mn\text{-}dis}$ is the release rate of solid Nd (${}^iNd_{MnO_2}$) in MnO_2 during reduction ($RMnO_{2_{red}}$).

In this formulation, newly formed oxides have the same ε_{Nd} as the pore water precipitating them, and during dissolution the release of dissolved Nd isotopes are proportional to the release of dissolved Mn according to the solid concentration ratio of Nd isotopes to Mn in MnO_2 (*i.e.*, dissolution is congruent).

3.2. Authigenic phosphate

We consider the precipitation-dissolution of rhabdophane ($NdPO_4$) using the classic linear Transient State Theory (TST) (Steefel et al., 2014):

$$R^iNd_{PO_4} = k_{NdPO_4} \times a^iNdPO_4 \times ([{}^iNd^{3+}] \times [PO_4^{3-}]/K_{sp_{NdPO_4}}/a^iNdPO_4 - 1), \quad (4)$$

where

k_{NdPO_4} is the precipitation rate constant;

a^iNdPO_4 is the activity of the isotopic $NdPO_4$ species (i=143,144), which we assume to form an ideal solid-solution so that the activity is equal to the mole fraction;

$[{}^iNd^{3+}]$ is the *free* Nd concentration of an isotope;

$[PO_4^{3-}]$ is the concentration of PO_4^{3-} ion;

$K_{sp_{NdPO_4}}$ is the *apparent* solubility.

Positive $R^{i}Nd_{PO_4}$ favors precipitation while negative values imply dissolution. This formulation ensures that newly formed $NdPO_4$ has the same ε_{Nd} as the pore water.

3.3. Marine silicate weathering

We model the dissolution of four silicate phases: basalt glass, clinopyroxene, plagioclase and chlorite. The general TST law of silicate dissolution is (Heřmanská et al., 2022):

$$R_{silicate} = k_{silicate} \times S_{silicate} \times M_{silicate} \times silicate \times (1 - \Omega_{silicate}), \quad (5)$$

Which is used for clinopyroxene and chlorite, but modified for basalt and plagioclase to include the Al-inhibition term (Heřmanská et al., 2022):

$$R_{basalt} = k_{basalt} \times S_{basalt} \times M_{basalt} \times basalt \times (a^3_{H^+}/a_{Al^{3+}})^{1/3} \times (1 - \Omega_{basalt}), \quad (6)$$

$$R_{plag} = k_{plag} \times S_{plag} \times M_{plag} \times plag \times (a^3_{H^+}/a_{Al^{3+}})^{0.35} \times (1 - \Omega_{plag}), \quad (7)$$

where

k is the surface area normalized Si release rate;

S is the specific surface area;

M is the mineral molecular weight;

Silicate/Basalt/Plag is the mineral concentration in solid sediment;

Ω is the saturation state in pore water, and dissolution is allowed only when $\Omega<1$;

a refers to aqueous activity.

The release of Nd isotopes are assumed congruent to Si:

$$R^{143}Nd_{silicate} = R_{silicate} \times r_{Nd/Si} \times 0.35971 \times {}^{143}Nd/{}^{144}Nd_{silicate}/({}^{143}Nd/{}^{144}Nd_{silicate} + 1), \quad (8)$$

$$R^{144}Nd_{silicate} = R_{silicate} \times r_{Nd/Si} \times 0.35971/({}^{143}Nd/{}^{144}Nd_{silicate} + 1), \quad (9)$$

where

$r_{Nd/Si}$ is the molar Nd/Si ratio in silicates;

$^{143}Nd/^{144}Nd_{silicate}$ is the Nd isotopic ratio of silicates.

3.4. Reverse weathering

In the model, reverse weathering includes two reactions: (1) opal dissolution, releasing dissolved Si to pore water, and; (2) authigenic illite formation, previously identified in marine sediments (Mackin and Aller, 1986), that consumes cations and alkalinity from pore water while releasing CO_2. The net reaction is:

$$3.15SiO_2 + 2.85Al(OH)_3 + 0.85K^+ + 0.85HCO_3^- \rightarrow K_{0.85}Al_{2.85}Si_{3.15}O_{10}(OH)_2 + 0.85CO_2 + 3.7H_2O, \quad (10)$$

Opal dissolution also releases Al according to a molar Al/Si ratio of 0.0025 in diatom frustules (Van Cappellen et al., 2002), and marine silicate weathering provides additional Al sources.

The dissolution rate of opal is (Van Cappellen et al., 2002):

$$R_{opal} = k_{opal} \times opal \times (1 - \Omega_{opal}), \quad (11)$$

where

k_{opal} is the opal dissolution rate constant and,

Ω_{opal} is the opal saturation state.

The rate of authigenic illite precipitation is computed using the TST rate law Eq. (5) when $\Omega_{illite}>1$.

3.5. Model simulations

We perform two types of simulations: baseline simulations and simulations that further add silicate weathering and reverse weathering. The baseline simulations include the sediment biogeochemical reactions and the authigenic Fe/Mn oxides and phosphate phases, and we test both the reversible scavenging and co-precipitation formulations. In the silicate weathering and reverse weathering simulations, silicate phases are added to the sediments to study their behavior. We test the model sensitivity to the dissolution rates of silicates, and the precipitation rates of authigenic clay during reverse weathering.

The model domain is the top 50 cm of the sediment, representing ~3500 years of sedimentation. This depth domain is discretized into 200 intervals, with finer grid spacing close to SWI to capture the large biogeochemical gradients there, resulting in 6600 coupled and stiff differential equations in the baseline simulations. Boundary conditions and the model solution are described in the Supplementary Methods.

4. Results

4.1. Sediment biogeochemistry

The model reproduces the classic redox sequence at site HH3000 (Fig. 2). The depth-integrated OC remineralization rate is 0.5 mmol/m^2/d, typical of this margin at similar water depth (McManus et al., 2012). The remineralization pathway is dominated by aerobic respiration (37.6%) and sulfate reduction (52.6%) (Fig. 2a). Despite its importance, sulfate reduction is still far from complete, with only ~0.5 mM of SO_4 consumed in the top 50 cm (Fig. 2f) and little formation of Fe sulfides (~0.12 wt%, Fig. 2e). Denitrification (8.0%) and MnO_2 reduction (1.6%) also contribute to carbon remineralization, but there is little FeOOH reduction (0.25%) and methanogenesis is negligible (Fig. 2a). Organic carbon respiration slightly decreases pH from ~7.7 in the bottom water to ~7.3 in the deep pore water (Fig. 2i). Pore water total silica concentration is relatively high (~620 μM, Fig. 2g) because of high opal content.

In the model, the surface bioturbated layer is ~ 6 cm thick. To fit the OC profile (Fig. 2d), the initial age of OC in the continuum reactivity model is 60 yr, higher than that of fresh phytoplankton but within the range observed in deep-sea studies (Arndt et al., 2013). To fit the dissolved phosphate profile (Fig. 2h), the required P/C ratio is 1/170, lower than the classic Redfield ratio (1/106). Together, the lower reactivity and P/C imply the presence of refractory terrestrial OC at this site (Hastings et al., 2012).

Assuming sediments below 6 cm represent the lithogenic background, the excesses of MnO_2, presumably authigenic, are ~0.45 wt% near the surface (Fig. 2d) (Abbott et al., 2016). Modeled surface sediment MnO_2 (~0.05 wt%) has to be lower than this value to fit the pore water Mn profile (Fig. 2c), suggesting that the surface enrichment might be a transient feature, or that other interfaces or microbial processes are involved but not modeled. Estimated authigenic (0.5 wt%) and modeled (0.2 wt%) FeOOH are similar (Fig. 2d). The authigenic enrichment of Fe is thus much lower than Mn, given the higher lithogenic background for Fe (~5 wt%) versus Mn (~0.07 wt%). Model results are consistent with elemental mapping using energy dispersive X-ray spectroscopy (EDS), which shows that Fe is located mainly in silicates, while Mn is enriched in amorphous nanoparticles that are likely authigenic (Abbott et al., 2019). Modeled Mn cycling is more intense than Fe cycling, at rates one order of magnitude higher for Mn than Fe (Fig. 2d). The modeled benthic Mn flux is 0.14 μmol/m^2/d, in the range of measurements at similar depths at this margin

(McManus et al., 2012). The modeled benthic Fe flux is –0.005 μmol/m^2/d, also consistent with measurements (McManus et al., 1997).

5. Discussion

5.1. Authigenesis

Authigenesis has typically been considered the main process affecting the early diagenesis of REE (Haley et al., 2004; German and Elderfield, 1989), which in turn has justified the assumption that pore water and authigenic Nd are simply derived from bottom water Nd at the SWI (Goldstein and Hemming, 2003). Here we investigate to what degree authigenesis alone can explain the observations of the diagenetic Nd cycle.

5.1.1. Authigenic Fe/Mn oxides and co-precipitation

Our co-precipitation formulation is controlled by the partition coefficients (D). We use the results of the GEOTRACES Pacific GP16 cruise (Haley et al., 2021; Lam et al., 2018) to derive these parameter values. $D_{Nd/Mn}$ is calculated as $(Nd_{auth}/MnO_2)/(Nd_d/Mn_d)$. Nd_{auth} is the measured particulate Nd corrected for lithogenic background, using a lithogenic Nd/Al mass ratio of 3.375×10^{-4} and measured particulate Al. Data for authigenic MnO_2, FeOOH, dissolved Nd and Mn are from the cited studies (Haley et al., 2021; Lam et al., 2018). We find $D_{Nd/Mn}$=0.025 and $D_{Nd/Fe}$=0.005 in the deep-sea (>2500 m). Using these values, the fluxes of Nd carried by MnO_2 and FeOOH into sediments at the study site are 612 and 40 pmol/cm^2/yr, respectively, based on the MnO_2 and FeOOH fluxes in the model (Supplementary Information).

For co-precipitation, the modeled pore water and authigenic Nd agree well with measurements (Fig. 3). MnO_2 reduction (by POC, Fe^{2+} and H_2S) is predicted to be the major source of pore water Nd (Fig. 3d), while Mn oxidation (by O_2) is a small sink. The depth-integrated MnO_2 reduction source (647 pmol Nd/cm^2/yr) far outweighs the Mn oxidation sink (35 pmol Nd/cm^2/yr). In comparison, FeOOH reduction (by POC and H_2S) is a much smaller source of pore water Nd (Fig. 3d), while Fe oxidation (by O_2 and MnO_2) is a relatively larger sink. The depth-integrated FeOOH reduction source (120 pmol Nd/cm^2/yr) slightly exceeds the Fe oxidation sink (80 pmol Nd/cm^2/yr).

5.1.2. Authigenic Fe/Mn oxides and reversible scavenging

The reversible scavenging formulation is controlled by the adsorption constants (K_{ads}). We use values of $K_{ads\text{-}MnO2}$=5×10^7 (M^{-1}) and $K_{ads\text{-}FeOOH}$=0.8×10^7 (M^{-1}), to deliver the same amount of Nd to the sediment via Fe/Mn oxides as in the co-precipitation simulation (Supplementary Methods).

These model results cannot explain the pore water Nd profile (Fig. 4). Modeled peak Nd concentration is far deeper than measured (Fig. 4c). Model sensitivity tests show that by varying K_{ads} the magnitude of the peak Nd concentration would change, but it would not affect the depth of the peak (Supplementary Fig. 1). This is because, in the presence of MnO_2 and FeOOH, Nd remains in the adsorbed form, and is converted to dissolved Nd only when the concentrations of oxides greatly decrease (Fig. 4b). In contrast, in the co-precipitation formulation Nd is released to pore water as soon as oxide reduction begins (Fig. 3d). The failure of reversible scavenging is perhaps not surprising given that *reversible* adsorption is a first step toward *irreversible* structural incorporation (co-precipitation), and laboratory experiments have identified the gradual structural incorporation of adsorbed trace metals into Mn oxides (Atkins et al., 2016).

Most existing ocean models rely on reversible scavenging to explain increasing seawater REE (and other TEIs) concentrations with increasing water depth in the open ocean (Arsouze et al., 2009; Siddall et al., 2008), on the premise that the concentrations of particulate scavengers decrease with depth. However, no ocean REE model has included Fe/Mn oxides, despite the fact that they are amongst the most important scavengers, especially in the deep ocean (Schijf et al., 2015). If Fe/Mn oxide concentrations in seawater increase with depth, as recent GEOTRACES results have shown (Lam et al., 2018), reversible scavenging onto Fe/Mn oxides would predict a decrease, rather than an increase, of seawater REE concentrations with depth. Our results do not necessarily indicate that adsorption is unimportant, but rather that the reversible scavenging formulation in present ocean models may be unsuitable to describe this process, or that kinetic rather than equilibrium process may better describe particulate-dissolved interaction in seawater. We suggest that future studies need to include Fe/Mn oxides to robustly evaluate the appropriateness of reversible scavenging.

5.1.3. Authigenic phosphate

Solid REE concentrations in Pacific sediments are most strongly correlated to phosphate, more so than Fe/Mn oxides and other elements (Bi et al., 2021). Also, bio-apatite becomes strongly enriched in REE post-deposition (Toyoda and Tokonami, 1990). Diagenetic Nd formed on foraminiferal tests is associated with oxides, *but also phosphorous* (Roberts et al., 2012). Transformation of labile Fe/Mn oxide-associated REE to stable phosphate phases has been identified in pelagic sediments, suggesting phosphate is likely the ultimate sink of REE (Takahashi et al., 2015). Whether REE form their own phosphate minerals, are incorporated into authigenic Ca-phosphates, or are taken up by biogenic phosphate, is unclear. In the model, we choose rhabdophane, a common REE mineral forming in low-temperature environment (Gausse et al., 2016; Liu and Byrne, 1997; Pearce et al., 2013), as the authigenic phosphate ($NdPO_4$), largely because relevant thermodynamic data exist.

Literature values of $\log({K_{sp}}^{0}_{NdPO_4})$ at standard state and zero ionic strength are in the range of –26 ~ –24 (Gausse et al., 2016). The corresponding *apparent* $\log(K_{sp_{NdPO_4}})$ in seawater medium at *in situ* temperature (2ºC) and atmospheric pressure is estimated to be –20 ~ –18 using the activity coefficients of Pierrot and Millero (2017), but we lack the thermodynamic data to compute the constant at *in situ* pressure. Model sensitivity tests show that the higher end of solubility estimates fits the pore water Nd profile better (Supplementary Fig. 2), which could be because either greater pressure leads to higher solubility than reported values at the standard state, or because $NdPO_4$ formed in sediments is less crystalline than the versions used in some solubility experiments (Gausse et al., 2016). The saturation concentration of *total* Nd with respect to $NdPO_4$ is

$$Nd_{saturation} = K_{sp_{NdPO_4}}/([PO_4^{3-}] \times f_{Nd^{3+}}), \quad (12)$$

where $f_{Nd^{3+}}$ is the fraction of the *free* Nd^{3+} ion.

Given k_{NdPO_4} = 100 pmol/cm^3/yr, the modeled pore water Nd fits observations very well (Fig. 3g). Pore water becomes oversaturated below ~1 cm. Close to the SWI, solid $NdPO_4$ that is formed in the over-saturation zone beneath is brought up to the under-saturation zone by bioturbation, and its dissolution is a greater source of pore water Nd than MnO_2 reduction (Fig. 3d, e). Overall, phosphate precipitation is the

dominant sink of pore water Nd, far surpassing that of Fe/Mn oxidation (Fig. 3d–e). As modeled oxides disappear below 30 cm, the model predicts pore water Nd concentration that are nearly at *equilibrium* with $NdPO_4$ (Fig. 3g). The modeled total (MnO_2, FeOOH and phosphate related) authigenic Nd concentration (~9 ppm) also matches estimates based on an *operationally* defined acid-reductive leaching (Abbott et al., 2016). Though leaching studies of authigenic Nd have traditionally focused on the role of Fe/Mn oxides, it is well-known that the acetic acid used in these studies can also extract authigenic and biogenic phosphates (Ruttenberg, 1992).

5.1.4. Authigenesis and benthic flux

The benthic Nd flux in the model is affected by molecular diffusion and bio-irrigation (i.e., convective exchange between pore water and bottom water due to the activity of benthic organisms) (Supplementary Methods). Using the co-precipitation formulation and including authigenic phosphate, the modeled diffusive flux is 39 pmol/cm^2/yr, agreeing well with the estimate (24~41 pmol/cm^2/yr) based on the measured pore water profile (Abbott et al., 2015b). The model uses the bio-irrigation parameterization of Meile and Van Cappellen (2003), derived from the globally measured O_2 flux. The resulting bio-irrigation Nd flux is 20 pmol/cm^2/yr. This value is an upper limit because the impact of bio-irrigation on other dissolved species is likely weaker than on O_2 (Meile et al., 2005). Taken together the total benthic flux is 59 pmol/cm^2/yr.

The authigenic minerals influence the benthic Nd flux in different ways. Both MnO_2 and $NdPO_4$ are sources of pore water Nd at the SWI, and thus support the benthic flux. However, when integrated over the sediment column, MnO_2 is a net source of pore water Nd while $NdPO_4$ is a net sink (Fig. 3d–f). In contrast, FeOOH is a sink of pore water Nd at the SWI and thus decreases the benthic flux (Fig. 3d–f), despite the fact that FeOOH is a net source of pore water Nd integrated over the sediment column.

In summary, in the baseline simulation including only authigenesis, the early diagenetic Nd cycle at the study site can be described as near total (~91%) conversion of Nd carried by incoming MnO_2, and to a lesser degree FeOOH, to authigenic $NdPO_4$, with a small fraction (~9%) returning to bottom water via diffusion and irrigation. Since, in this model, all Nd sources ultimately come from incoming water column-derived Fe/Mn oxides, modeled pore water and authigenic ε_{Nd} are the same as bottom water (Fig. 3i).

5.2. Silicate weathering

The observed relatively small ε_{Nd} difference (+0.6 ε) between pore water and bottom water is an indication that bottom water ε_{Nd} is strongly influenced by pore water ε_{Nd} because of a large benthic flux (Abbott et al., 2016). To explain this difference additional processes must be invoked. Much larger differences between pore water/authigenic and bottom water ε_{Nd} exist elsewhere, linked to smaller benthic flux or reactive lithogenic sediments (Abbott et al., 2016; Blaser et al., 2019; Du et al., 2016; Wilson et al., 2013). Moreover, variations in authigenic ε_{Nd} on glacial-interglacial timescales is only on the order of 1~2 ε, sometimes correlated to changes of lithogenic sediment ε_{Nd} (Du et al., 2020 and references therein). It is thus important to understand ε_{Nd} differences on this order of magnitude for robust circulation reconstruction.

5.2.1. The reactive spectrum of silicate minerals

Our next model iteration investigates the impact of marine silicate weathering on the diagenetic cycle of ε_{Nd}, focusing on mineral reactivity. We model four phases: basaltic glass, clinopyroxene, chlorite and plagioclase (albite): all present in the study region (Abbott et al., 2019; VanLaningham et al., 2008). Volcanic glass, often derived from ash deposition that reaches far into the ocean interior, is ubiquitous in Pacific sediments (Du et al., 2020; Straub and Schmincke, 1998). Clinopyroxene is a mafic mineral that is commonly found in sediments near volcanic arcs. Chlorite often exists as a clay mineral, as the metamorphic alteration production of igneous minerals (Griffin et al., 1968). Plagioclase is not necessarily volcanic but it is the most abundant primary silicate mineral, after quartz, in marine sediments (Li and Schoonmaker, 2014). Collectively they represent a large range of silicate reactivity in terms of abundance, dissolution rate and solubility.

We add these phases separately to the baseline model, with deposition fluxes that are proportional to the total incoming sediment: 2 wt% of basalt glass and clinopyroxene, 10 wt% of chlorite and 20 wt% of plagioclase respectively, based on published abundance data in the study region (Abbott et al., 2019; VanLaningham et al., 2008; Zemmels and Cook, 1973). Interrogation of the GEOROC database (Supplementary Methods), either using data from the Cascade Arc or other convergent margins, suggests that the average Nd/Si molar ratios of basalt glass, clinopyroxene and plagioclase are 1.9×10^{-5}, 1.8×10^{-5} and 1.9×10^{-6} respectively (Supplementary Fig. 3), consistent with the partition coefficients of Nd in silicates

(Taylor and McLennan, 1988). For chlorite, we use the average Nd/Si ratio (1.6×10^{-5}) of clay minerals from rivers draining volcanic terrains, as compiled by Bayon et al., (2015). In comparison, the average Nd/Si ratio of volcanic rocks from the Cascade Arc is 1.7×10^{-5}, similar to that of basalt glass, clinopyroxene and clay, but 1-order of magnitude higher than plagioclase. The average ε_{Nd} of Cascade volcanic rocks is +6.2 ε which we use for all four silicates. Dissolution parameters for these phases are reported in Supplementary Table 6.

We further assume that during silicate weathering the Nd/Si dissolution rate ratio is the same as the Nd/Si ratio in silicates (*i.e.*, congruent dissolution). In the laboratory dissolution experiment of Pearce et al., (2013), the ratio of *gross* Nd/Si release, estimated using ε_{Nd}, from three basalt samples at the end of 121 days is ~2.5×10^{-5}. This value is similar to the Nd/Si ratio in their basalt samples (~2.1×10^{-5}), supporting our assumption. No other experimental studies of Nd and ε_{Nd} during silicate dissolution exists to our knowledge, thus whether this assumption is true for other silicates is presently not tested.

Field-derived weathering rates are often lower than laboratory-derived values, a conundrum that has been attributed to inadequate dissolution rate laws, the loss of reactive surface sites due to occlusion, fluid transport limitation and the influence of secondary phases on saturation state (e.g., Maher et al., 2006). For example, Maher et al., (2006) suggested that the plagioclase dissolution rate in deep-sea sediments is 10^5 times lower than in the laboratory for the linear TST rate law at their study site. To investigate our model sensitivity, we vary the silicate dissolution rates by 6 orders of magnitude, from the laboratory-derived rates to values 1 to 5 orders of magnitude lower.

At higher dissolution rates, silicates are quickly consumed, while at lower rates greater amounts of minerals are preserved (Fig. 5). The modeled pore water Nd concentration, however, do not respond linearly to changes of dissolution rate (Fig. 5–6). In the upper sediment (<10 cm), dissolved Nd still largely agrees with the observed concentrations (Fig. 6), as silicate Nd release at even the highest dissolution rates are slower than Nd release from MnO_2/$NdPO_4$ (Fig. 3). In the deeper sediment, modeled dissolved Nd exceeds the measured values at intermediate dissolution rates, but neither with the highest nor lowest rates: the former because the silicates are spent and the latter because dissolution is slow at all depths. Modeled dissolved Si is subject to a similar influence (Fig. 5).

Model sensitivity also depends on mineral abundance, Nd/Si ratio and solubility (Fig. 5–6). Modeled Nd, Si concentrations and ε_{Nd} are not sensitive to dissolution of basaltic glass nor clinopyroxene because their Nd and Si reservoirs are small due to low abundance at the study site (Fig. 5a–h, 6a–h). In contrast, modeled Si concentration are very sensitive to plagioclase dissolution (Fig. 5i–l) because it is more abundant and thus has greater potential to affect pore water chemistry, such as pH. This in turn drives large changes of Nd speciation and dissolved Nd concentration (Fig. 6i). The influence on ε_{Nd} is however limited too because low Nd/Si in plagioclase leads to a small Nd reservoir. In comparison, despite a relatively high abundance and large Nd reservoir, modeled ε_{Nd} is not much more sensitive to chlorite dissolution rates because of its relatively low solubility (Fig. 5m–p, 6m–p).

5.2.2. Best-fit silicate weathering models

Considering the fit to observed pore water ε_{Nd}, Nd and Si concentrations, the best-fit models include the weathering of volcanic phases such as basaltic glass and clinopyroxene, at dissolution rates within 2 orders of magnitude of laboratory-derived rates (Fig. 5a–h, 6a–h), and with their presence at <2 wt%. This relatively high reactivity may be explained by their "freshness," because of direct volcanic ash deposition, or fast physical erosion of volcanic rocks in the Costal Range and Cascade Arc, coupled to short transport times in coastal rivers and efficient dispersal of fluvial sediments on the Oregon margin (Wheatcroft and Sommerfield, 2005). In contrast, to explain pore water ε_{Nd} requires that nearly all plagioclase dissolves, inconsistent with its observed abundance at ~20 wt%. The model using chlorite cannot fit Nd concentration and ε_{Nd} simultaneously, and its abundance at ~10 wt% also suggest it is likely not reactive. The inferred low reactivity of plagioclase and chlorite implies that at site HH3000 these minerals are probably not of volcanic origin (*i.e.*, sedimentary or metamorphic), and have experienced loss of reactivity before reaching the seafloor.

Adding silicate weathering increases *diffusive* benthic Nd fluxes from 39 pmol/cm^2/yr in the baseline model to 41~42 pmol/cm^2/yr in the best-fit models (the range is given for basalt weathering using dissolution rates that are 10^{-1}~10^{0} times of laboratory-derived rate). Thus, the impact of silicate weathering on the elemental Nd benthic flux is likely non-measurable at site HH3000. In contrast, the ε_{Nd} of the flux increases from –2.4 ε to –1.7~ –1.3 ε, a significant difference given the analytical uncertainty (2σ=0.27 ε).

Modeled pore water ε_{Nd} is more radiogenic than bottom water (–2.4 ε), and importantly, the trend of pore water ε_{Nd} deviating toward bottom water ε_{Nd} at ~5 cm is reproduced (Fig. 6c, 6g). This depth is where MnO_2 reduction rate is at a maximum, and thus is the peak release for seawater derived Nd (Fig. 3d).

Modeled authigenic ε_{Nd} is similar to pore water, but has a smoother profile (Fig. 6d, 6h), as authigenic phases integrate over longer timescales and are subject to bioturbation. However, modeled authigenic ε_{Nd} is still not as radiogenic as the *operationally* defined leachate ε_{Nd} (Abbott et al., 2016), suggesting that the leach likely extracts some non-authigenic components that are refractory under *in situ* sediment conditions but reactive in laboratory leaching (Abbott et al., 2022, 2016; Du et al., 2016). If the lower pH and wash off of major cations during leaching increases the dissolution rates and under-saturation of silicate minerals like plagioclase and chlorite, enough silicate Nd could be released, just as our model demonstrates (Fig. 6p). At site HH3000, a combination of ~8.5 ppm *truly* authigenic Nd (–1.8 ε) with ~0.5 ppm Nd extracted from silicates (+6.2 ε), can explain the leachate Nd (~9 ppm and ~ –1.2 ε).

5.3.Reverse weathering

Authigenic clay formation during reverse weathering can affect the saturation state of primary silicates by influencing pore water Al concentration (Maher et al., 2006), thus *indirectly* controlling the diagenetic Nd cycle. In the "best-fit" silicate weathering models discussed above, we included reverse weathering using an authigenic illite precipitation rate of 10^{-19} mol/m^2/s, as suggested by a previous study (Maher et al., 2006), but ~6 orders of magnitude lower than laboratory-derived rates (Marty et al., 2015).

We ran further sensitivity tests of the influence of reverse weathering by varying the authigenic illite precipitation rate (Fig. 7): 10^{-19} mol/m^2/s in the "normal clay" model; 10^{-16} in the "fast clay"; 10^{-22} in the "slow clay", and 0 in the "no clay" (no reverse weathering) models. At the study site illite is also a *detrital* mineral through riverine input (VanLaningham et al., 2008). Therefore, in the model, we add a *detrital* illite flux that represents 2 wt% of the total sediment. We model the *total* illite concentration, with the *authigenic* fraction as the excess above the detrital input. In these tests we include basalt weathering as discussed previously, at a dissolution rate 10^{-1} times the laboratory-derived value.

Close to the SWI (<0.2 cm), modeled Al and Si concentrations are positively correlated because of co-release by basalt and opal dissolution, but they become anti-correlated at depth because of authigenic

illite formation, except in the "no clay" model wherein the positive correlation persists (Fig. 7e–f, 8). At depth, the Al concentration converges to equilibrium values with respect to illite solubility in the "fast clay" model, but reaches an asymptote to values that are congruent to Si with respect to opal in the "no clay" model. Pore water Al in the upper sediment increases from ~1 nM in the "fast clay" model to ~1000 nM in the "no clay" model (Fig. 7e), reducing basalt under-saturation, until over-saturation (Fig. 7g). Authigenic illite concentration is <1 wt% in all models.

Pore water Al was not measured at HH3000. We compare the modeled Al-Si relationship with published seawater and pore water data to evaluate if model results are reasonable (Fig. 8). Al-Si trends in the "fast clay" and "normal clay" models follow that of deep ocean water (GEOTRACES Intermediate Data Product Group, 2021) and East China Sea pore water (Mackin and Aller, 1984). Al-Si trends in the "normal clay" and "slow clay" models bracket pore water data from the North Atlantic, Southern Ocean and Amazon shelf (Mackin and Aller, 1986, 1986; Stoffyn-Egli, 1982; Van Beueskom et al., 1997). The Al speciation in the model considers only hydrolysis, but if other ligands are present, which is likely in reality, then the same *free* Al^{3+} concentration in the model would lead to greater *total* Al concentrations. Thus the modeled total Al concentration is likely a lower limit. Overall, we consider the "normal clay" model the best option given its consistency with literature data and the uncertainty in Al speciation. As long as the precipitation rate is higher than in the "slow clay" model, reverse weathering will drive basalt weathering, and modeled pore water ε_{Nd} will agree with observations (Fig. 7l).

Finally, whether Nd is *directly* incorporated into authigenic clay is unknown. If it is, and assuming the same Nd/Si ratio as primary silicates, the authigenic illite sink for Nd (<3 pmol/cm^3/yr) (Fig. 7a) would be much smaller than the phosphate sink (~200 pmol/cm^3/yr) (Fig. 3d), and thus negligible.

6. Implications and perspectives

The modeled diagenetic Nd cycle at the study site is summarized in Fig. 9. Our aim was to investigate the roles of commonly suggested sedimentary processes, rather than comprehensively consider all potential processes. That the model successfully simulated observations indicates co-cycling with Fe/Mn, authigenic phosphate formation, silicate weathering and reverse weathering are indeed among the most

important at the study site. Future studies should aim to examine other potential processes, such as the role of organic ligands and colloids in pore water.

Our study paves the way for modeling diagenetic Nd cycling at other sites and regions where the relative contributions of the studied processes may differ. For instance, site HH200 on the Oregon shelf (200 m) has a much larger pore water to bottom water ε_{Nd} difference (+1.6 ε) than the study site HH3000 (+0.6 ε), corresponding to a greater abundance of volcanic phases like glass and clinopyroxene in sediments (Abbott et al., 2019). One would thus expect silicate weathering to be more important than at the deep-sea site HH3000.

Our study also has global implications. With authigenesis alone, a benthic flux only produces regenerated Nd (Fig. 9), with significant impact on the oceanic budget of Nd concentration but not ε_{Nd}. In contrast, silicate weathering produces a new external source of Nd (Fig. 9), which may have a small impact on the Nd concentration but a significant one on ε_{Nd}, particularly when the ε_{Nd} difference between seawater and reactive silicate phases is large. This contrast in element versus isotopic sensitivity mirrors seawater observations and implies that diagenetic transformation at the SWI is likely a key component of Boundary Exchange (Jeandel, 2016). The apparent conservative behavior of seawater ε_{Nd}, in the presence of non-conservative Nd concentration due to benthic flux, can be preserved in the first case but not in the second. The reality is likely somewhere in-between (Du et al., 2020). We suggest the differing response of Nd concentration versus ε_{Nd} to the benthic flux is key to resolving the "Nd paradox" (Goldstein and Hemming, 2003).

Our results may also explain why, globally, benthic Nd fluxes do not correlate to redox parameters such as bottom water oxygen and OC rain rate (Du et al., 2018). For example, strong redox cycling on the continental shelf does not convert to high benthic Nd flux (Abbott et al., 2015b; Deng et al., 2022) as it does for Fe and Mn (McManus et al., 2012, 1997). We suggest that the non-redox-sensitive Nd sink (phosphate) may play a more important role than the redox-sensitive source (Fe/Mn oxides). If phosphate precipitation/dissolution is fast enough, pore water Nd concentrations will be largely controlled by phosphate solubility, and only weakly dependent on redox cycling.

Our model illustrates the *indispensable* role of pore water TEI data in constraining diagenetic processes and fluxes across the SWI. In our best-fit models, with 2 wt% basalt/clinopyroxene supply to sediments, only <0.4 wt% remains at the surface, and none below 10 cm. Such small fractions are virtually undetectable by solid phase analysis methods, let alone when the solid phases have disappeared completely and leave only an imprint on pore water. Thus, it is likely *not* possible to study such processes using solid phase analysis alone: pore water TEIs may be our only source of evidence.

The processes investigated here also affect the diagenesis of other TEIs (Little et al., 2020; Jeandel, 2016). Presently, the application of diagenetic modeling to TEIs is limited by the scarcity of comprehensive pore water data and measurements of the fluxes of all solid components into sediments. As fluxes at the SWI are increasingly seen to be a key part of the global ocean budgets of TEIs (Homoky et al., 2016), it is important for further pore water and sediment trap TEI studies, as extensions of the GEOTRACES water column surveys.

7. Conclusions

We created the first reactive-transport model for Nd and ε_{Nd} in marine sediments, and quantified the roles of authigenesis, silicate weathering and reverse weathering in the early diagenetic Nd cycle at the deep-sea site HH3000 on the Oregon margin.

The model correctly captured the biogeochemical processes at the site and successfully simulated the observed pore water Nd profile using the co-precipitation formulation of Nd co-cycling with Fe/Mn and authigenic phosphate formation. In the simulation, we found that MnO_2 reduction is the main source of Nd in pore water, phosphate formation is the main sink, and Fe cycling plays a minor role. Benthic Nd flux is mainly driven by MnO_2 reduction and phosphate dissolution close to the SWI. In contrast, the model cannot reproduce the pore water Nd profile via the reversible scavenging formulation of Nd co-cycling with Fe/Mn.

We further included silicate weathering and reverse weathering to simulate pore water ε_{Nd}. We studied the model's sensitivity to the dissolution of basaltic glass, clinopyroxene, plagioclase and chlorite, representing a wide range of mineral reactivity, abundance and solubility. The model correctly simulated pore water ε_{Nd} (and other data) if it includes the weathering of basaltic glass or clinopyroxene with relatively

high dissolution rates, supporting the hypothesis that weathering of volcanic sediments is responsible for the relatively more radiogenic ε_{Nd} of pore water and authigenic phases in the Pacific. Furthermore, we show that reverse weathering is necessary to maintain relatively low pore water Al concentrations, thus enabling the undersaturation of primary silicates and indirectly contributing to the diagenetic Nd cycle.

Acknowledgements

This project has received funding from the European Union's Horizon 2020 research and innovation programme under the Marie Skłodowska-Curie grant agreement 891489. J.D. was also supported by an ETH Zurich Postdoctoral Fellowship 19-2 FEL-32. A.C.M and B.A.H. received funding from US NSF Grant 1357529. B.A.H was supported by US NSF Grant 1850765. J.M. was supported by US NSF Grant 1850789. Collection of Oregon margin pore water and sediment data were funded by US NSF Grant 1147407. We thank Dr. Laurence Coogan for editorial handling, and Dr. Catherine Jeandel and one other anonymous reviewer for their comments and insights which greatly improved this manuscript.

Data availability

Model output from this study can be found at: https://doi.org/10.5281/zenodo.6998239.

Figure legends

Fig 1. Map of the study region. Site HH3000 is marked by the white dot with black border. The two thin black lines on the seafloor indicate the 200 m and 3000 m depth contours. The white dashed lines indicate the plate tectonic boundaries. The red triangles on land indicate volcanoes in the Cascades. The blue lines on land indicate rivers.

Fig. 2. Modeled sediment biogeochemistry. (a) POC oxidation rates. (b) Mn and Fe cycling rates. (c–h) Solid and dissolved species (lines) compared with measured values (colored dots with red borders). (i) Pore water pH (free proton scale). The prefix "T" in names indicates total concentrations summed over all species (e.g., $TH_3PO_4 = H_3PO_4 + H_2PO_4^- + HPO_4^{2-} + PO_4^{3-}$).

Fig. 3. Baseline simulation using the co-precipitation formulation for Fe/Mn oxides and including $NdPO_4$. (a–c) Fe, Mn and phosphate cycling. (d) Nd uptake/release due to individual reactions. Positive means Nd release to pore water and negative uptake. (e) Net Nd release/uptake driven by Fe, Mn and phosphate cycling. (f) pore water Nd sources and sinks summed over individual reactions, and the net source. (g) Concentrations of the *total* dissolved Nd and the *free* Nd^{3+} ion, and the *total* Nd concentrations at saturation with respect to $NdPO_4$. (h) Authigenic Nd concentrations. (i) Pore water and authigenic ε_{Nd}. In the plots colored dots with red borders indicate direct measurements, except in (h–i) where authigenic Nd and ε_{Nd} are estimated using an *operationally* defined acid-reductive leach.

Fig. 4. Model results using the reversible scavenging formulation of Fe/Mn oxides. (a) Fe/Mn oxide concentrations. (b) Nd adsorbed on to the oxides. (c) Pore water Nd concentrations compared with the results of the co-precipitation formulation and with measurements (in red dots). Sensitivity tests involving different adsorption constants are reported in Supplementary Fig. 1.

Fig. 5. Model sensitivity to silicate dissolution rate. (a) Nd release rate by basalt dissolution. (b) Basalt concentration. (c) Dissolved silica. Red dots indicate measurements. (d) Basalt saturation index. Red dashed line indicates saturation. The color legend in (a) indicates the orders of magnitude of dissolution rate reduction in the sensitivity tests. "1e0" means dissolution rate is the same as the laboratory-derived value. "1e1" means a dissolution rate that is 1-order of magnitude lower etc. (e–h) are the same as (a–d) but for clinopyroxene. (i–l) are for plagioclase, and (m–p) are for chlorite.

Fig. 6. Sensitivity of the Nd cycle to silicate weathering. (a–d) Pore water Nd, authigenic Nd, pore water ε_{Nd}, and authigenic ε_{Nd} respectively in the basalt weathering sensitivity tests. The color legend in (a) indicates the orders of magnitude of dissolution rate reduction in the sensitivity tests as in Fig. 5. Red dots indicate direct measurements, except that authigenic Nd and ε_{Nd} are estimated using an *operationally* defined acid-

552 reductive leach. In (c–d) the 2σ analytical errors of ε_{Nd} are shown. (e–h), (i–l) and (m–p) are the results of
553 model tests with weathering of clinopyroxene, plagioclase and chlorite respectively.

554

555 Fig. 7. The impact of reverse weathering on silicate weathering and the Nd cycle. (a) Illite precipitation rate.
556 (b) Basalt dissolution rate. (c) Opal dissolution rate. (d) pH. (e) Al concentration. (f) Dissolved Si. (g) Basalt
557 saturation index. Dash red line indicates saturation. (h) Illite saturation index. (i) Basalt concentration. (j)
558 Authigenic illite concentration. (k) Pore water Nd. (l) Pore water ε_{Nd}. The color legend in (a) indicates the
559 sensitivity tests using different authigenic clay precipitation rates. Red dots indicate measured values.

560

561 Fig. 8. Modeled pore water Al-Si relationship at the study site compared with literature results. Seawater
562 data are from the GEOTRACES IDP2021 (GEOTRACES Intermediate Data Product Group, 2021) and only
563 the deep ocean data are shown (>1000 m depth). Pore water data are from the North Atlantic, Southern
564 Ocean, East China Sea and Amazon shelf (Mackin and Aller, 1986, 1986; Stoffyn-Egli, 1982; Van
565 Beueskom et al., 1997). Al and Si concentrations are in units of mol/kg on the log scale.

566

567 Fig. 9. Summary of the early diagenetic cycle of Nd and ε_{Nd} at HH3000. Black italic numbers are Nd fluxes
568 and depth-integrated transformation rates in pmol/cm^2/yr. The benthic fluxes are written in the form of
569 "diffusive + bio-irrigation" fluxes. Purple numbers are ε_{Nd}. The summary is based on (1) the baseline model
570 using the co-precipitation formulation of Fe/Mn oxides and including authigenic phosphate, (2) the silicate-
571 weathering model using the dissolution of basalt glass at a rate 1 order of magnitude lower than laboratory-
572 derived rate, and (3) the "normal clay" model of reverse weathering. Reverse weathering is shown in dashed
573 lines as it influences the Nd cycle indirectly by driving the marine silicate weathering. The flux of refractory
574 silicate Nd is not modeled but calculated using the sedimentation rate and refractory silicate Nd
575 concentration, which is estimated as the difference between the measured bulk and modeled authigenic Nd
576 concentration. Similarly, the ε_{Nd} of refractory silicate is computed using the measured bulk ε_{Nd} and modeled
577 authigenic ε_{Nd} based on isotopic mass balance. The refractory silicates are not reactive on the short timescale

of early diagenesis but may become reactive on the longer timescales of later diagenesis. Bulk sediment data are from Abbott et al., (2016).

Reference

Abbott, A.N., Haley, B.A., McManus, J., 2016. The impact of sedimentary coatings on the diagenetic Nd flux. Earth and Planetary Science Letters 449, 217–227. https://doi.org/10.1016/j.epsl.2016.06.001

Abbott, A.N., Haley, B.A., McManus, J., 2015a. Bottoms up: Sedimentary control of the deep North Pacific Ocean's εNd signature. Geology 43, 1035–1035. https://doi.org/10.1130/G37114.1

Abbott, A.N., Haley, B.A., McManus, J., Reimers, C.E., 2015b. The sedimentary flux of dissolved rare earth elements to the ocean. Geochimica et Cosmochimica Acta 154, 186–200. https://doi.org/10.1016/j.gca.2015.01.010

Abbott, A.N., Löhr, S., Trethewy, M., 2019. Are Clay Minerals the Primary Control on the Oceanic Rare Earth Element Budget? Front. Mar. Sci. 6. https://doi.org/10.3389/fmars.2019.00504

Abbott, A.N., Löhr, S.C., Payne, A., Kumar, H., Du, J., 2022. Widespread lithogenic control of marine authigenic neodymium isotope records? Implications for paleoceanographic reconstructions. Geochimica et Cosmochimica Acta 319, 318–336. https://doi.org/10.1016/j.gca.2021.11.021

Aller, R.C., 2014. Sedimentary Diagenesis, Depositional Environments, and Benthic Fluxes, in: Holland, H.D., Turekian, K.K. (Eds.), Treatise on Geochemistry (Second Edition). Elsevier, Oxford, pp. 293–334.

Arndt, S., Jørgensen, B.B., LaRowe, D.E., Middelburg, J.J., Pancost, R.D., Regnier, P., 2013. Quantifying the degradation of organic matter in marine sediments: A review and synthesis. Earth-Science Reviews 123, 53–86. https://doi.org/10.1016/j.earscirev.2013.02.008

Arsouze, T., Dutay, J.-C., Lacan, F., Jeandel, C., 2009. Reconstructing the Nd oceanic cycle using a coupled dynamical – biogeochemical model. Biogeosciences 6, 2829–2846. https://doi.org/10.5194/bg-6-2829-2009

Atkins, A.L., Shaw, S., Peacock, C.L., 2016. Release of Ni from birnessite during transformation of birnessite to todorokite: Implications for Ni cycling in marine sediments. Geochimica et Cosmochimica Acta 189, 158–183. https://doi.org/10.1016/j.gca.2016.06.007

Bayon, G., Toucanne, S., Skonieczny, C., André, L., Bermell, S., Cheron, S., Dennielou, B., Etoubleau, J., Freslon, N., Gauchery, T., Germain, Y., Jorry, S.J., Ménot, G., Monin, L., Ponzevera, E., Rouget, M.-L., Tachikawa, K., Barrat, J.A., 2015. Rare earth elements and neodymium isotopes in world river sediments revisited. Geochimica et Cosmochimica Acta 170, 17–38. https://doi.org/10.1016/j.gca.2015.08.001

Bertram, C.J., Elderfield, H., 1993. The geochemical balance of the rare earth elements and neodymium isotopes in the oceans. Geochimica et Cosmochimica Acta 57, 1957–1986. https://doi.org/10.1016/0016-7037(93)90087-D

Bi, D., Shi, X., Huang, M., Yu, M., Zhou, T., Zhang, Y., Zhu, A., Shi, M., Fang, X., 2021. Geochemical and mineralogical characteristics of deep-sea sediments from the western North Pacific Ocean: Constraints on the enrichment processes of rare earth elements. Ore Geology Reviews 138, 104318. https://doi.org/10.1016/j.oregeorev.2021.104318

Blaser, P., Pöppelmeier, F., Schulz, H., Gutjahr, M., Frank, M., Lippold, J., Heinrich, H., Link, J.M., Hoffmann, J., Szidat, S., Frank, N., 2019. The resilience and sensitivity of Northeast Atlantic deep water εNd to overprinting by detrital fluxes over the past 30,000 years. Geochimica et Cosmochimica Acta 245, 79–97. https://doi.org/10.1016/j.gca.2018.10.018

Boudreau, B.P., 1997. Diagenetic models and their implementation : modelling transport and reactions in aquatic sediments. Springer, Berlin; New York.

Deng, K., Yang, S., Du, J., Lian, E., Vance, D., 2022. Dominance of benthic flux of REEs on continental shelves: implications for oceanic budgets. Geochemical Perspectives Letters 22, 26–30. https://doi.org/10.7185/geochemlet.2223

Du, J., Haley, B.A., Mix, A.C., 2020. Evolution of the Global Overturning Circulation since the Last Glacial Maximum based on marine authigenic neodymium isotopes. Quaternary Science Reviews 241, 106396. https://doi.org/10.1016/j.quascirev.2020.106396

Du, J., Haley, B.A., Mix, A.C., 2016. Neodymium isotopes in authigenic phases, bottom waters and detrital sediments in the Gulf of Alaska and their implications for paleo-circulation reconstruction. Geochimica et Cosmochimica Acta 193, 14–35. https://doi.org/10.1016/j.gca.2016.08.005

Du, J., Haley, B.A., Mix, A.C., Walczak, M.H., Praetorius, S.K., 2018. Flushing of the deep Pacific Ocean and the deglacial rise of atmospheric CO 2 concentrations. Nature Geoscience 11, 749–755. https://doi.org/10.1038/s41561-018-0205-6

Elderfield, H., Greaves, M.J., 1982. The rare earth elements in seawater. Nature 296, 214–219. https://doi.org/10.1038/296214a0

Gausse, C., Szenknect, S., Qin, D.W., Mesbah, A., Clavier, N., Neumeier, S., Bosbach, D., Dacheux, N., 2016. Determination of the Solubility of Rhabdophanes LnPO4·0.667H2O (Ln = La to Dy). European Journal of Inorganic Chemistry 2016, 4615–4630. https://doi.org/10.1002/ejic.201600517

GEOTRACES Intermediate Data Product Group, 2021. The GEOTRACES Intermediate Data Product 2021 (IDP2021). NERC EDS British Oceanographic Data Centre NOC. https://doi.org/10.5285/cf2d9ba9-d51d-3b7c-e053-8486abc0f5fd

German, C.R., Elderfield, H., 1989. Rare earth elements in Saanich Inlet, British Columbia, a seasonally anoxic basin. Geochimica et Cosmochimica Acta 53, 2561–2571. https://doi.org/10.1016/0016-7037(89)90128-2

Goldstein, S.J., Jacobsen, S.B., 1988. Rare earth elements in river waters. Earth and Planetary Science Letters 89, 35–47. https://doi.org/10.1016/0012-821X(88)90031-3

Goldstein, S.L., Hemming, S.R., 2003. Long-lived Isotopic Tracers in Oceanography, Paleoceanography, and Ice-sheet Dynamics, in: Holland, H.D., Turekian, K.K. (Eds.), Treatise on Geochemistry. Pergamon, Oxford, pp. 453–489.

Grenier, M., Jeandel, C., Lacan, F., Vance, D., Venchiarutti, C., Cros, A., Cravatte, S., 2013. From the subtropics to the central equatorial Pacific Ocean: Neodymium isotopic composition and rare earth element concentration variations. Journal of Geophysical Research: Oceans 118, 592–618. https://doi.org/10.1029/2012JC008239

Griffin, J.J., Windom, H., Goldberg, E.D., 1968. The distribution of clay minerals in the World Ocean. Deep Sea Research and Oceanographic Abstracts 15, 433–459. https://doi.org/10.1016/0011-7471(68)90051-X

Haley, B.A., Du, J., Abbott, A.N., McManus, J., 2017. The Impact of Benthic Processes on Rare Earth Element and Neodymium Isotope Distributions in the Oceans. Frontiers in Marine Science 4. https://doi.org/10.3389/fmars.2017.00426

Haley, B.A., Klinkhammer, G.P., McManus, J., 2004. Rare earth elements in pore waters of marine sediments. Geochimica et Cosmochimica Acta 68, 1265–1279. https://doi.org/10.1016/j.gca.2003.09.012

Haley, B.A., Wu, Y., Muratli, J.M., Basak, C., Pena, L.D., Goldstein, S.L., 2021. Rare earth element and neodymium isotopes of the eastern US GEOTRACES Equatorial Pacific Zonal Transect (GP16). Earth and Planetary Science Letters 576, 117233. https://doi.org/10.1016/j.epsl.2021.117233

Hastings, R.H., Goñi, M.A., Wheatcroft, R.A., Borgeld, J.C., 2012. A terrestrial organic matter depocenter on a high-energy margin: The Umpqua River system, Oregon. Continental Shelf Research 39–40, 78–91. https://doi.org/10.1016/j.csr.2012.04.002

Heřmanská, M., Voigt, M.J., Marieni, C., Declercq, J., Oelkers, E.H., 2022. A comprehensive and internally consistent mineral dissolution rate database: Part I: Primary silicate minerals and glasses. Chemical Geology 120807. https://doi.org/10.1016/j.chemgeo.2022.120807

Homoky, W.B., Weber, T., Berelson, W.M., Conway, T.M., Henderson, G.M., Hulten, M. van, Jeandel, C., Severmann, S., Tagliabue, A., 2016. Quantifying trace element and isotope fluxes at the ocean–sediment boundary: a review. Phil. Trans. R. Soc. A 374, 20160246. https://doi.org/10.1098/rsta.2016.0246

Jeandel, C., 2016. Overview of the mechanisms that could explain the 'Boundary Exchange' at the land–ocean contact. Phil. Trans. R. Soc. A 374, 20150287. https://doi.org/10.1098/rsta.2015.0287

Jeandel, C., Oelkers, E.H., 2015. The influence of terrigenous particulate material dissolution on ocean chemistry and global element cycles. Chemical Geology 395, 50–66. https://doi.org/10.1016/j.chemgeo.2014.12.001

Lacan, F., Jeandel, C., 2005. Neodymium isotopes as a new tool for quantifying exchange fluxes at the continent–ocean interface. Earth and Planetary Science Letters 232, 245–257. https://doi.org/10.1016/j.epsl.2005.01.004

Lam, P.J., Lee, J.-M., Heller, M.I., Mehic, S., Xiang, Y., Bates, N.R., 2018. Size-fractionated distributions of suspended particle concentration and major phase composition from the U.S. GEOTRACES Eastern Pacific Zonal Transect (GP16). Marine Chemistry, The U.S.GEOTRACES Eastern Tropical Pacific Transect (GP16) 201, 90–107. https://doi.org/10.1016/j.marchem.2017.08.013

Lambelet, M., Flierdt, T. van de, Butler, E.C.V., Bowie, A.R., Rintoul, S.R., Watson, R.J., Remenyi, T., Lannuzel, D., Warner, M., Robinson, L.F., Bostock, H.C., Bradtmiller, L.I., 2018. The Neodymium Isotope Fingerprint of Adélie Coast Bottom Water. Geophysical Research Letters 45, 11,247-11,256. https://doi.org/10.1029/2018GL080074

Li, Y.-H., Schoonmaker, J.E., 2014. Chemical Composition and Mineralogy of Marine Sediments, in: Holland, H.D., Turekian, K.K. (Eds.), Treatise on Geochemistry (Second Edition). Elsevier, Oxford, pp. 1–32.

Little, S.H., Archer, C., McManus, J., Najorka, J., Wegorzewski, A.V., Vance, D., 2020. Towards balancing the oceanic Ni budget. Earth and Planetary Science Letters 547, 116461. https://doi.org/10.1016/j.epsl.2020.116461

Liu, X., Byrne, R.H., 1997. Rare earth and yttrium phosphate solubilities in aqueous solution. Geochimica et Cosmochimica Acta 61, 1625–1633. https://doi.org/10.1016/S0016-7037(97)00037-9

Lyle, M., Zahn, R., Prahl, F., Dymond, J., Collier, R., Pisias, N., Suess, E., 1992. Paleoproductivity and carbon burial across the California Current: The multitracers transect, 42°N. Paleoceanography 7, 251–272. https://doi.org/10.1029/92PA00696

Mackin, J.E., Aller, R.C., 1986. The effects of clay mineral reactions on dissolved Al distributions in sediments and waters of the Amazon continental shelf. Continental Shelf Research 6, 245–262. https://doi.org/10.1016/0278-4343(86)90063-4

Mackin, J.E., Aller, R.C., 1984. Dissolved Al in sediments and waters of the East China Sea: Implications for authigenic mineral formation. Geochimica et Cosmochimica Acta 48, 281–297. https://doi.org/10.1016/0016-7037(84)90251-5

Maher, K., Steefel, C.I., DePaolo, D.J., Viani, B.E., 2006. The mineral dissolution rate conundrum: Insights from reactive transport modeling of U isotopes and pore fluid chemistry in marine sediments. Geochimica et Cosmochimica Acta 70, 337–363. https://doi.org/10.1016/j.gca.2005.09.001

Marty, N.C.M., Claret, F., Lassin, A., Tremosa, J., Blanc, P., Madé, B., Giffaut, E., Cochepin, B., Tournassat, C., 2015. A database of dissolution and precipitation rates for clay-rocks minerals. Applied Geochemistry, Geochemical Speciation Codes and Databases 55, 108–118. https://doi.org/10.1016/j.apgeochem.2014.10.012

McManus, J., Berelson, W.M., Coale, K.H., Johnson, K.S., Kilgore, T.E., 1997. Phosphorus regeneration in continental margin sediments. Geochimica et Cosmochimica Acta 61, 2891–2907. https://doi.org/10.1016/S0016-7037(97)00138-5

McManus, J., Berelson, W.M., Severmann, S., Johnson, K.S., Hammond, D.E., Roy, M., Coale, K.H., 2012. Benthic manganese fluxes along the Oregon–California continental shelf and slope. Continental Shelf Research 43, 71–85. https://doi.org/10.1016/j.csr.2012.04.016

Meile, C., Berg, P., Van Cappellen, P., Tuncay, K., 2005. Solute-specific pore water irrigation: Implications for chemical cycling in early diagenesis. J. Mar. Res. 63, 601–621. https://doi.org/10.1357/0022240054307885

Meile, C., Van Cappellen, P., 2003. Global estimates of enhanced solute transport in marine sediments. Limnol. Oceanogr. 48, 777–786. https://doi.org/10.4319/lo.2003.48.2.0777

Pearce, C.R., Jones, M.T., Oelkers, E.H., Pradoux, C., Jeandel, C., 2013. The effect of particulate dissolution on the neodymium (Nd) isotope and Rare Earth Element (REE) composition of seawater. Earth and Planetary Science Letters 369–370, 138–147. https://doi.org/10.1016/j.epsl.2013.03.023

Piepgras, D.J., Wasserburg, G.J., Dasch, E.J., 1979. The isotopic composition of Nd in different ocean masses. Earth and Planetary Science Letters 45, 223–236. https://doi.org/10.1016/0012-821X(79)90125-0

Pierrot, D., Millero, F.J., 2017. The Speciation of Metals in Natural Waters. Aquat Geochem 23, 1–20. https://doi.org/10.1007/s10498-016-9292-4

736 Roberts, N.L., Piotrowski, A.M., Elderfield, H., Eglinton, T.I., Lomas, M.W., 2012. Rare earth element
737 association with foraminifera. Geochimica et Cosmochimica Acta 94, 57–71.
738 https://doi.org/10.1016/j.gca.2012.07.009
739 Ruttenberg, K.C., 1992. Development of a sequential extraction method for different forms of phosphorus in
740 marine sediments. Limnology and Oceanography 37, 1460–1482.
741 https://doi.org/10.4319/lo.1992.37.7.1460
742 Schijf, J., Byrne, R.H., 2021. Speciation of yttrium and the rare earth elements in seawater: Review of a 20-
743 year analytical journey. Chemical Geology 584, 120479.
744 https://doi.org/10.1016/j.chemgeo.2021.120479
745 Schijf, J., Christenson, E.A., Byrne, R.H., 2015. YREE scavenging in seawater: A new look at an old model.
746 Marine Chemistry, Cycles of metals and carbon in the oceans - A tribute to the work stimulated by
747 Hein de Baar 177, 460–471. https://doi.org/10.1016/j.marchem.2015.06.010
748 Siddall, M., Khatiwala, S., van de Flierdt, T., Jones, K., Goldstein, S.L., Hemming, S., Anderson, R.F.,
749 2008. Towards explaining the Nd paradox using reversible scavenging in an ocean general
750 circulation model. Earth and Planetary Science Letters 274, 448–461.
751 https://doi.org/10.1016/j.epsl.2008.07.044
752 Steefel, C.I., Druhan, J.L., Maher, K., 2014. Modeling Coupled Chemical and Isotopic Equilibration Rates.
753 Procedia Earth and Planetary Science 10, 208–217. https://doi.org/10.1016/j.proeps.2014.08.022
754 Stoffyn-Egli, P., 1982. Dissolved aluminium in interstitial waters of recent terrigenous marine sediments
755 from the North Atlantic Ocean. Geochimica et Cosmochimica Acta 46, 1345–1352.
756 https://doi.org/10.1016/0016-7037(82)90270-8
757 Straub, S.M., Schmincke, H.U., 1998. Evaluating the tephra input into Pacific Ocean sediments: distribution
758 in space and time. Geol Rundsch 87, 461–476. https://doi.org/10.1007/s005310050222
759 Tachikawa, K., Athias, V., Jeandel, C., 2003. Neodymium budget in the modern ocean and paleo-
760 oceanographic implications. Journal of Geophysical Research: Oceans 108, 3254.
761 https://doi.org/10.1029/1999JC000285
762 Takahashi, Y., Hayasaka, Y., Morita, K., Kashiwabara, T., Nakada, R., Marcus, M.A., Kato, K., Tanaka, K.,
763 Shimizu, H., 2015. Transfer of rare earth elements (REE) from manganese oxides to phosphates
764 during early diagenesis in pelagic sediments inferred from REE patterns, X-ray absorption
765 spectroscopy, and chemical leaching method. GEOCHEMICAL JOURNAL 49, 653–674.
766 https://doi.org/10.2343/geochemj.2.0393
767 Taylor, S.R., McLennan, S.M., 1988. Chapter 79 The significance of the rare earths in geochemistry and
768 cosmochemistry, in: Handbook on the Physics and Chemistry of Rare Earths, Two-Hundred-Year
769 Impact of Rare Earths on Science. Elsevier, pp. 485–578. https://doi.org/10.1016/S0168-
770 1273(88)11011-8
771 Toyoda, K., Tokonami, M., 1990. Diffusion of rare-earth elements in fish teeth from deep-sea sediments.
772 Nature 345, 607–609. https://doi.org/10.1038/345607a0
773 Van Beueskom, J.E.E., Van Bennekom, A.J., Tréguer, P., Morvan, J., 1997. Aluminium and silicic acid in
774 water and sediments of the Enderby and Crozet Basins. Deep Sea Research Part II: Topical Studies
775 in Oceanography 44, 987–1003. https://doi.org/10.1016/S0967-0645(96)00105-1
776 Van Cappellen, P., Dixit, S., Beusekom, J. van, 2002. Biogenic silica dissolution in the oceans: Reconciling
777 experimental and field-based dissolution rates. Global Biogeochemical Cycles 16, 23-1-23–10.
778 https://doi.org/10.1029/2001GB001431
779 VanLaningham, S., Duncan, R.A., Pisias, N.G., Graham, D.W., 2008. Tracking fluvial response to climate
780 change in the Pacific Northwest: a combined provenance approach using Ar and Nd isotopic systems
781 on fine-grained sediments. Quaternary Science Reviews 27, 497–517.
782 https://doi.org/10.1016/j.quascirev.2007.10.018
783 Wheatcroft, R.A., Sommerfield, C.K., 2005. River sediment flux and shelf sediment accumulation rates on
784 the Pacific Northwest margin. Continental Shelf Research 25, 311–332.
785 https://doi.org/10.1016/j.csr.2004.10.001
786 Wilson, D.J., Piotrowski, A.M., Galy, A., Clegg, J.A., 2013. Reactivity of neodymium carriers in deep sea
787 sediments: Implications for boundary exchange and paleoceanography. Geochimica et
788 Cosmochimica Acta 109, 197–221. https://doi.org/10.1016/j.gca.2013.01.042
789 Zemmels, I., Cook, H.E., 1973. Appendix IV; X-ray mineralogy of sediments from the Northeast Pacific and
790 Gulf of Alaska-Leg 18 Deep Sea Drilling Project, in: Kulm, L.V.D., von Huene, R. (Eds.), Initial

Reports of the Deep Sea Drilling Project. U.S. Govt. Printing Office, Washington, D.C., pp. 1015–1060.

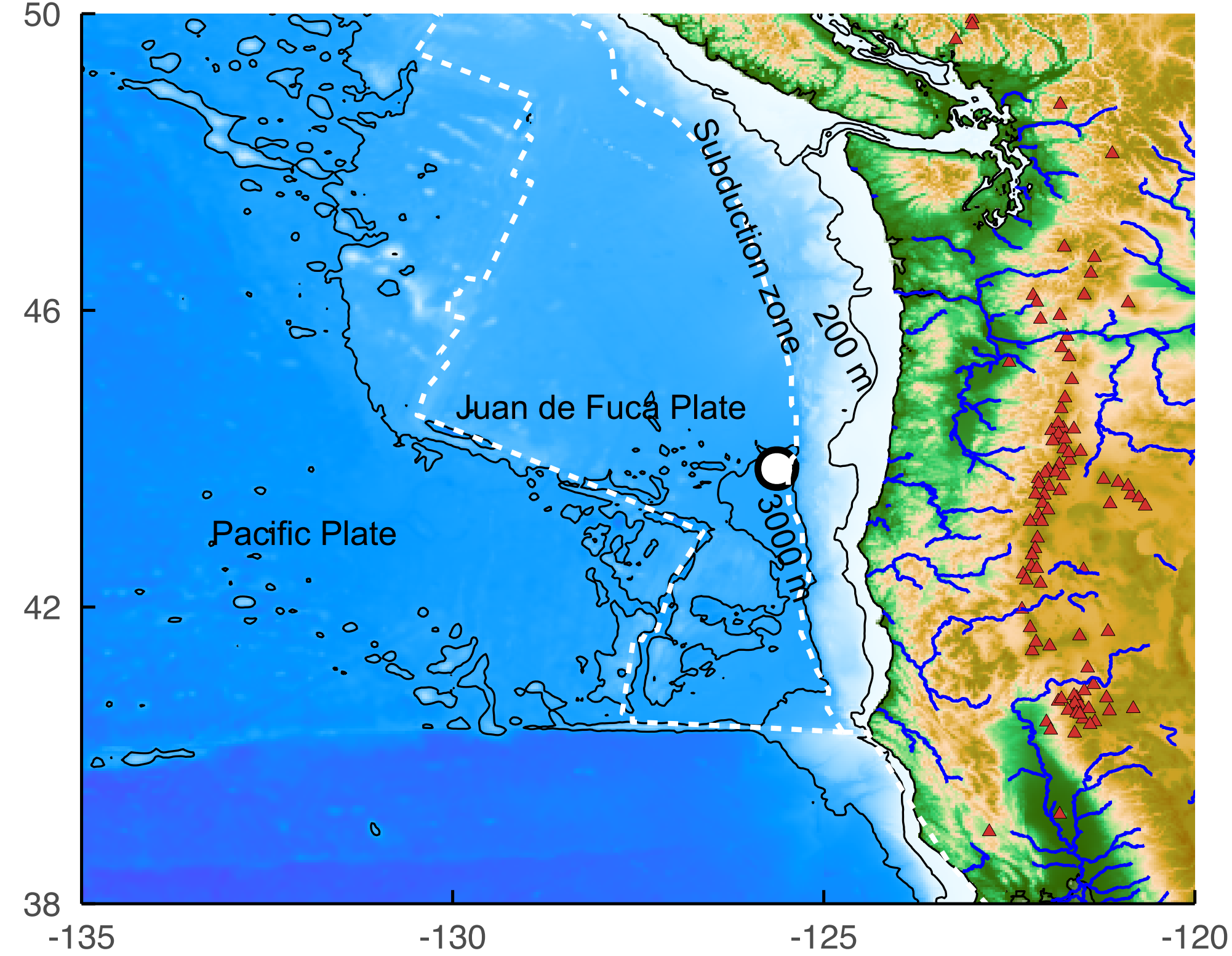
50
46
42
38
-135
-130
-125
-120
Subduction zone
200 m
3000 m
Juan de Fuca Plate
Pacific Plate

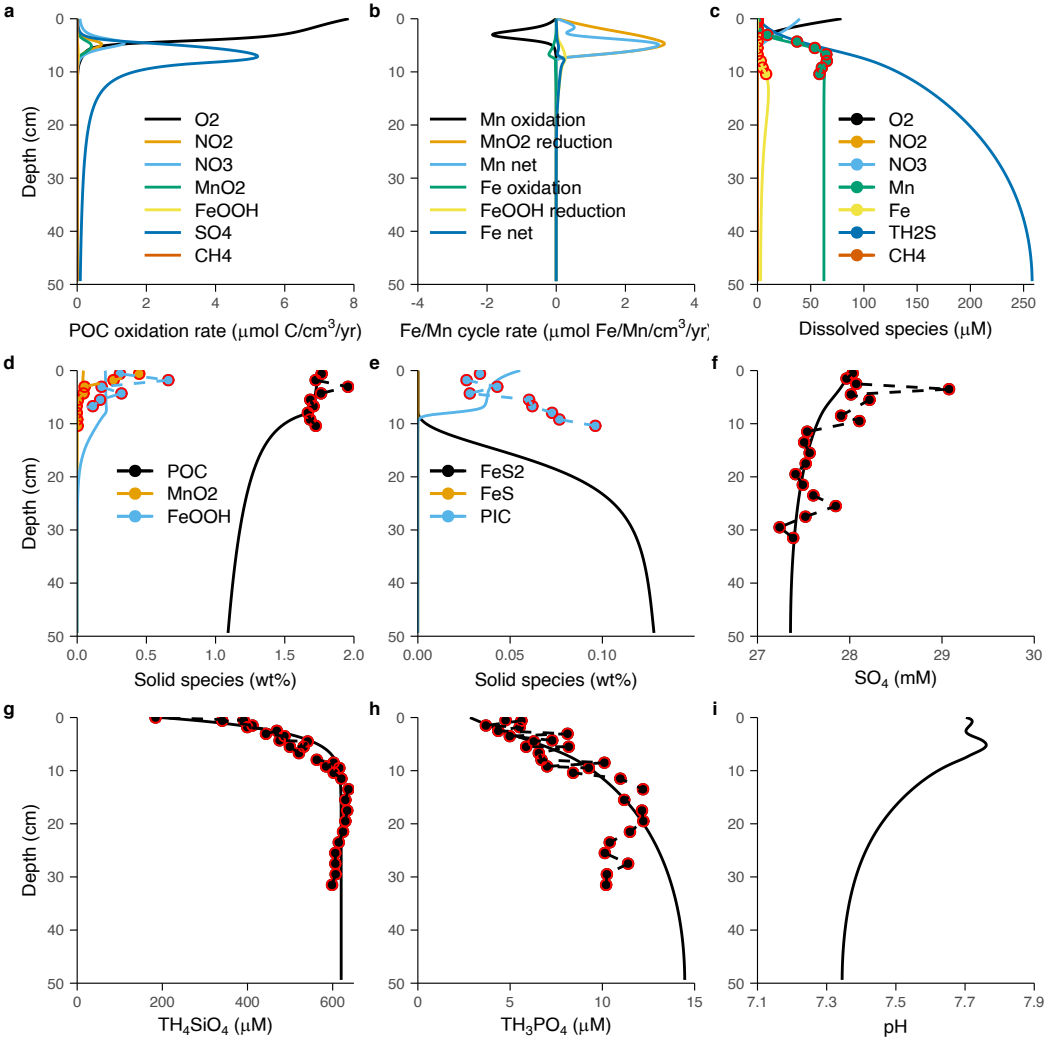
a
Depth (cm)
O2
NO2
NO3
MnO2
FeOOH
SO4
CH4
POC oxidation rate (μmol C/cm3/yr)
b
Mn oxidation
MnO2 reduction
Mn net
Fe oxidation
FeOOH reduction
Fe net
Fe/Mn cycle rate (μmol Fe/Mn/cm3/yr)
c
O2
NO2
NO3
Mn
Fe
TH2S
CH4
Dissolved species (μM)
d
POC
MnO2
FeOOH
Solid species (wt%)
e
FeS2
FeS
PIC
Solid species (wt%)
f
SO4 (mM)
g
TH4SiO4 (μM)
h
TH3PO4 (μM)
i
pH

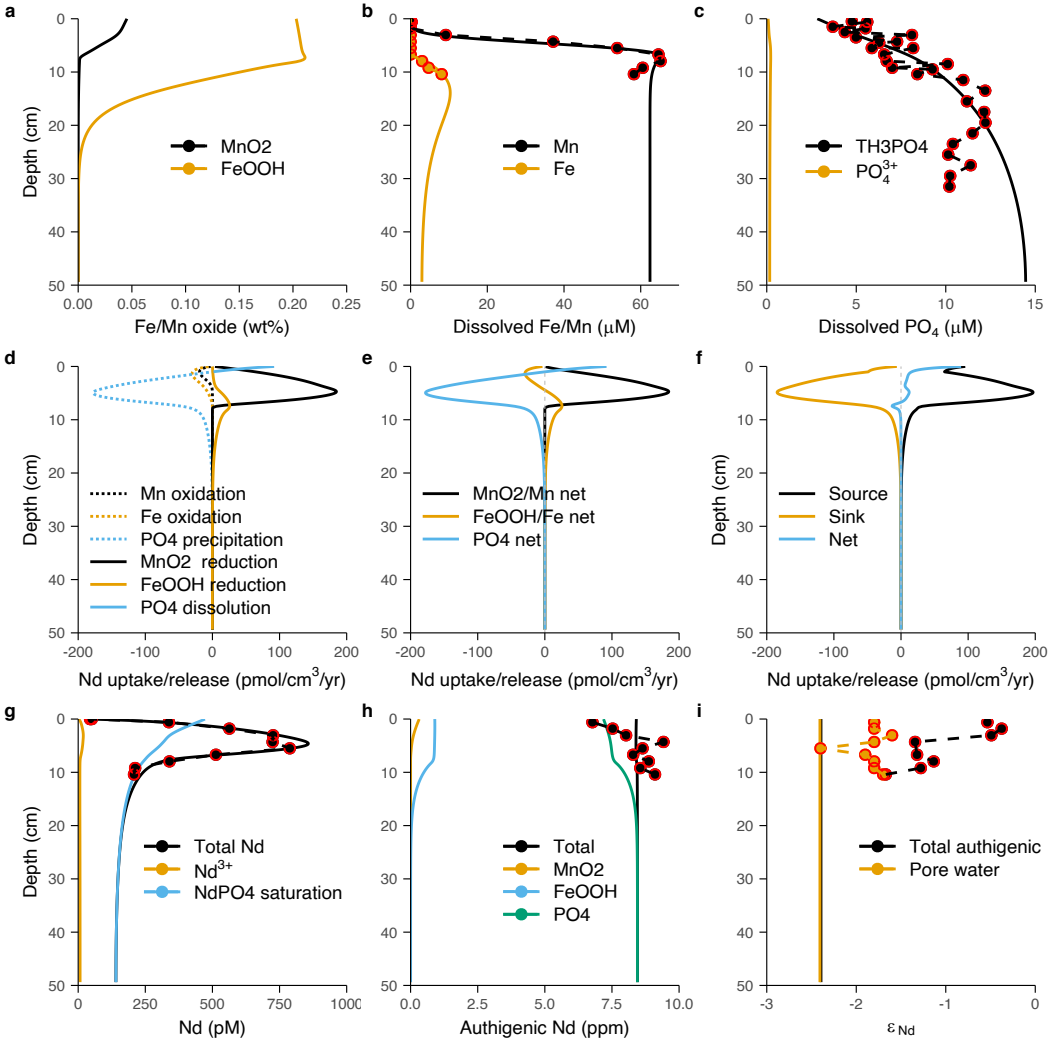
a
b
c
Depth (cm)
MnO2
FeOOH
Fe/Mn oxide (wt%)
Mn
Fe
Dissolved Fe/Mn (μM)
TH3PO4
PO43+
Dissolved PO4 (μM)
d
e
f
Mn oxidation
Fe oxidation
PO4 precipitation
MnO2 reduction
FeOOH reduction
PO4 dissolution
MnO2/Mn net
FeOOH/Fe net
PO4 net
Source
Sink
Net
Nd uptake/release (pmol/cm3/yr)
g
h
i
Total Nd
Nd3+
NdPO4 saturation
Nd (pM)
Total
MnO2
FeOOH
PO4
Authigenic Nd (ppm)
Total authigenic
Pore water
εNd

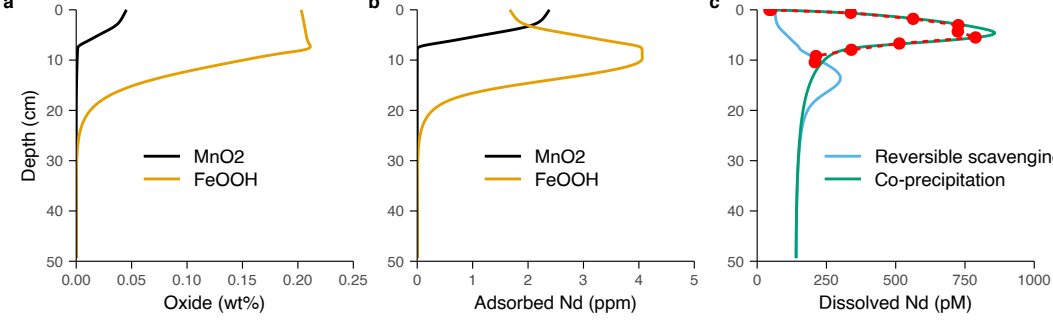
a
b
c
Depth (cm)
0
10
20
30
40
50
MnO2
FeOOH
0.00
0.05
0.10
0.15
0.20
0.25
Oxide (wt%)
0
1
2
3
4
5
Adsorbed Nd (ppm)
Reversible scavenging
Co-precipitation
0
250
500
750
1000
Dissolved Nd (pM)

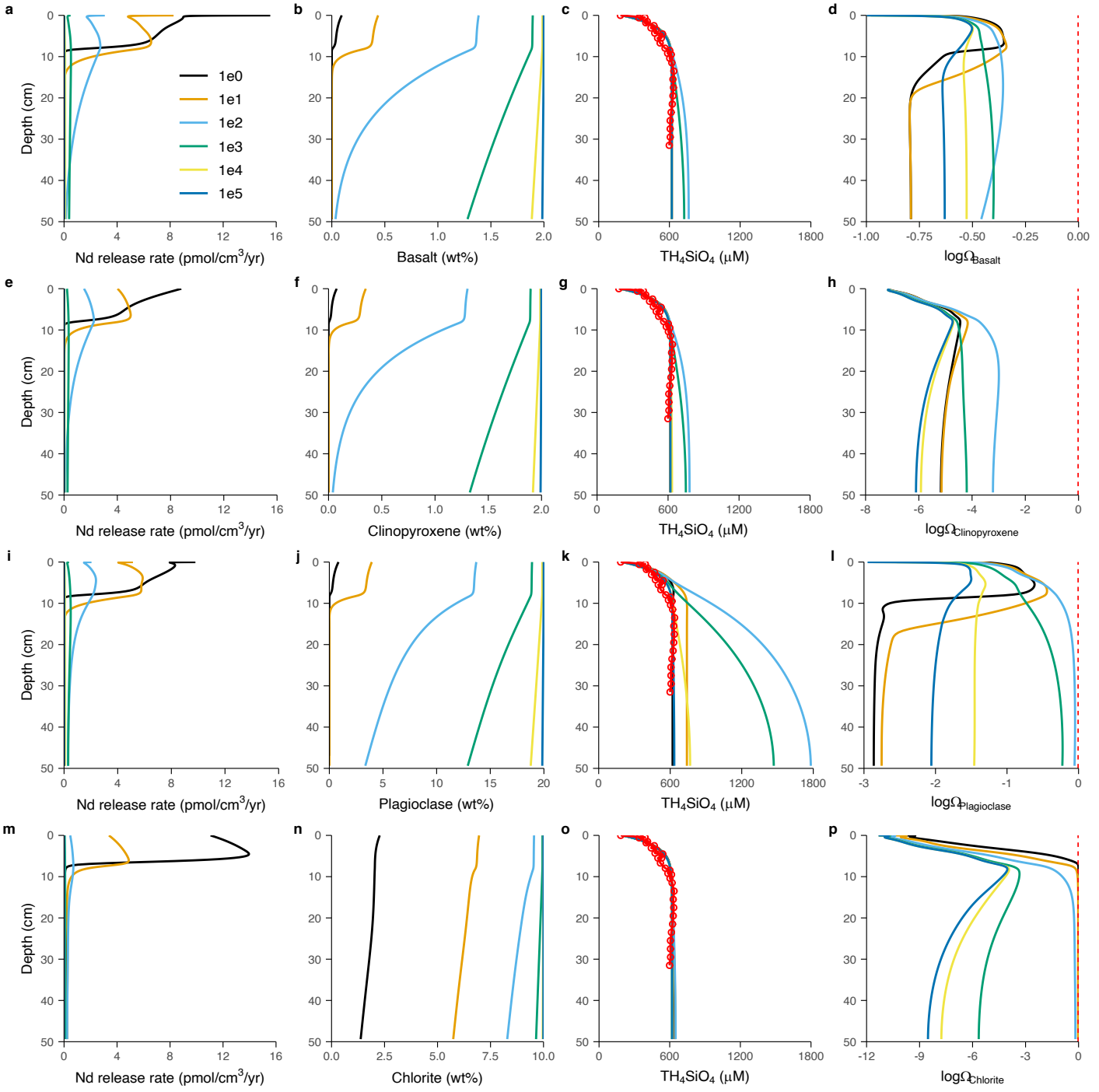
a
b
c
d
e
f
g
h
i
j
k
l
m
n
o
p
Depth (cm)
1e0
1e1
1e2
1e3
1e4
1e5
Nd release rate (pmol/cm3/yr)
Basalt (wt%)
TH4SiO4 (μM)
logΩBasalt
Clinopyroxene (wt%)
logΩClinopyroxene
Plagioclase (wt%)
logΩPlagioclase
Chlorite (wt%)
logΩChlorite

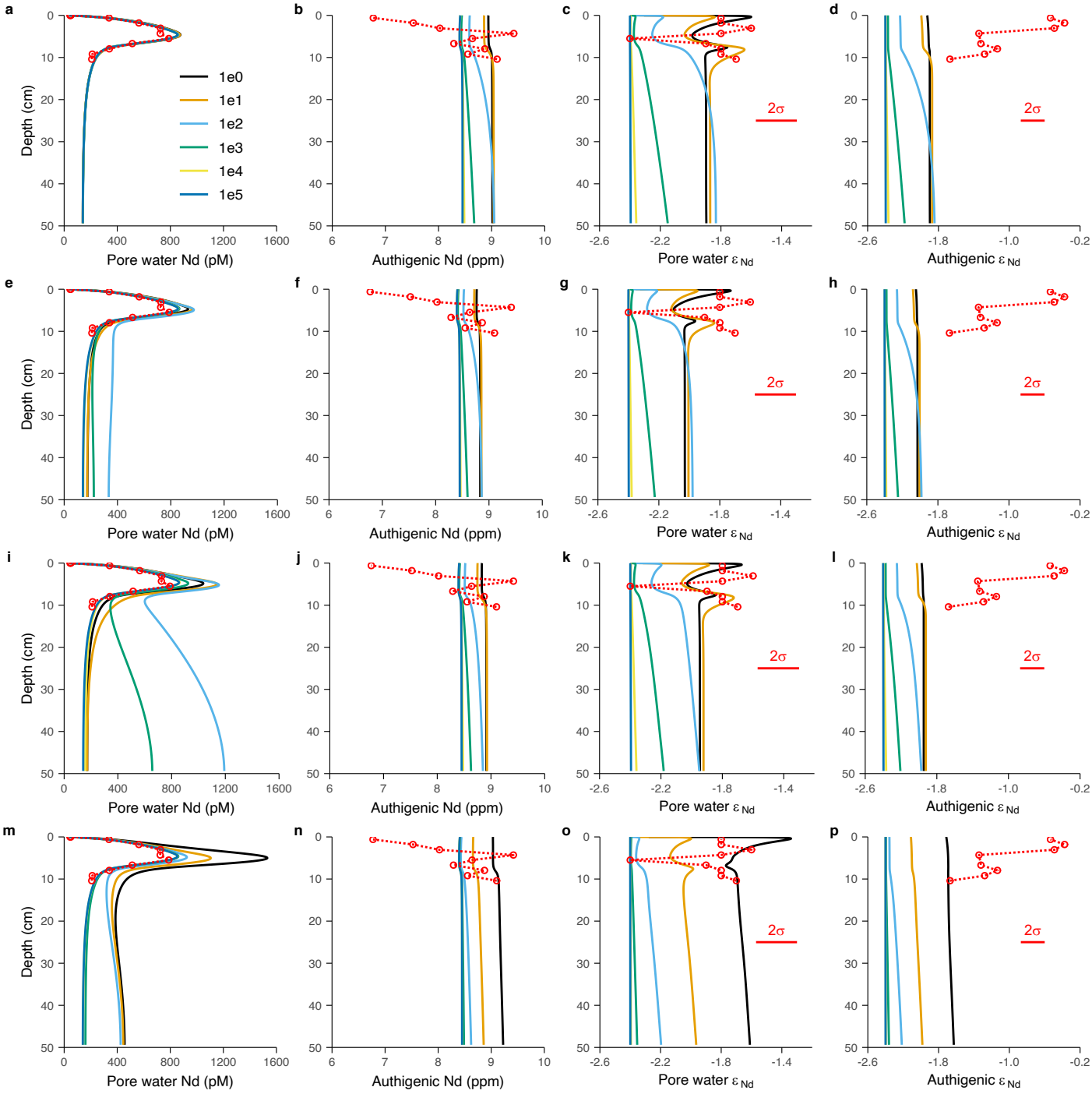
a
b
c
d
e
f
g
h
i
j
k
l
m
n
o
p
Depth (cm)
Pore water Nd (pM)
Authigenic Nd (ppm)
Pore water ε Nd
Authigenic ε Nd
1e0
1e1
1e2
1e3
1e4
1e5
2σ

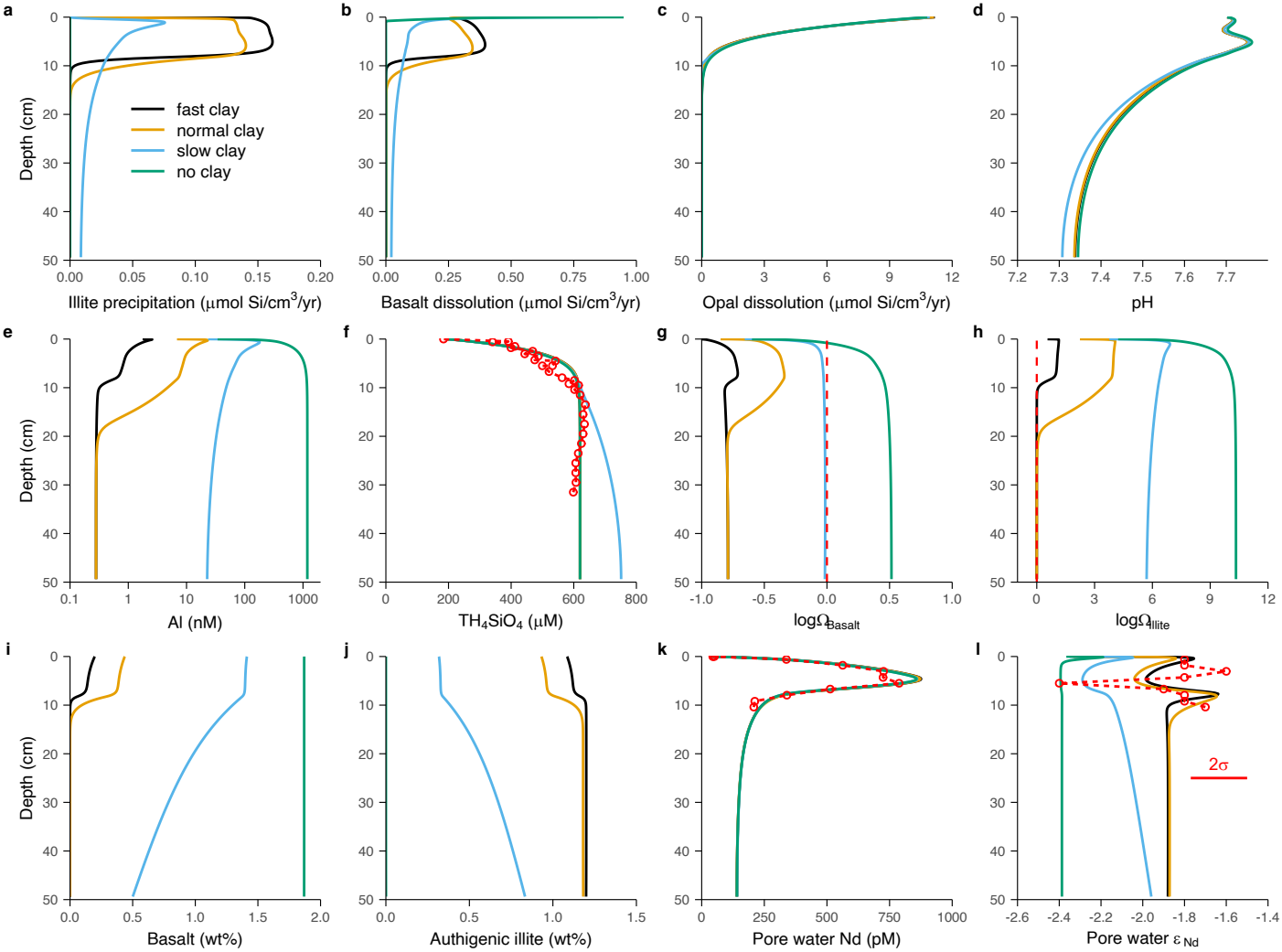
a
b
c
d
e
f
g
h
i
j
k
l
Depth (cm)
fast clay
normal clay
slow clay
no clay
Illite precipitation (μmol Si/cm3/yr)
Basalt dissolution (μmol Si/cm3/yr)
Opal dissolution (μmol Si/cm3/yr)
pH
Al (nM)
TH4SiO4 (μM)
logΩBasalt
logΩIllite
Basalt (wt%)
Authigenic illite (wt%)
Pore water Nd (pM)
Pore water εNd
2σ

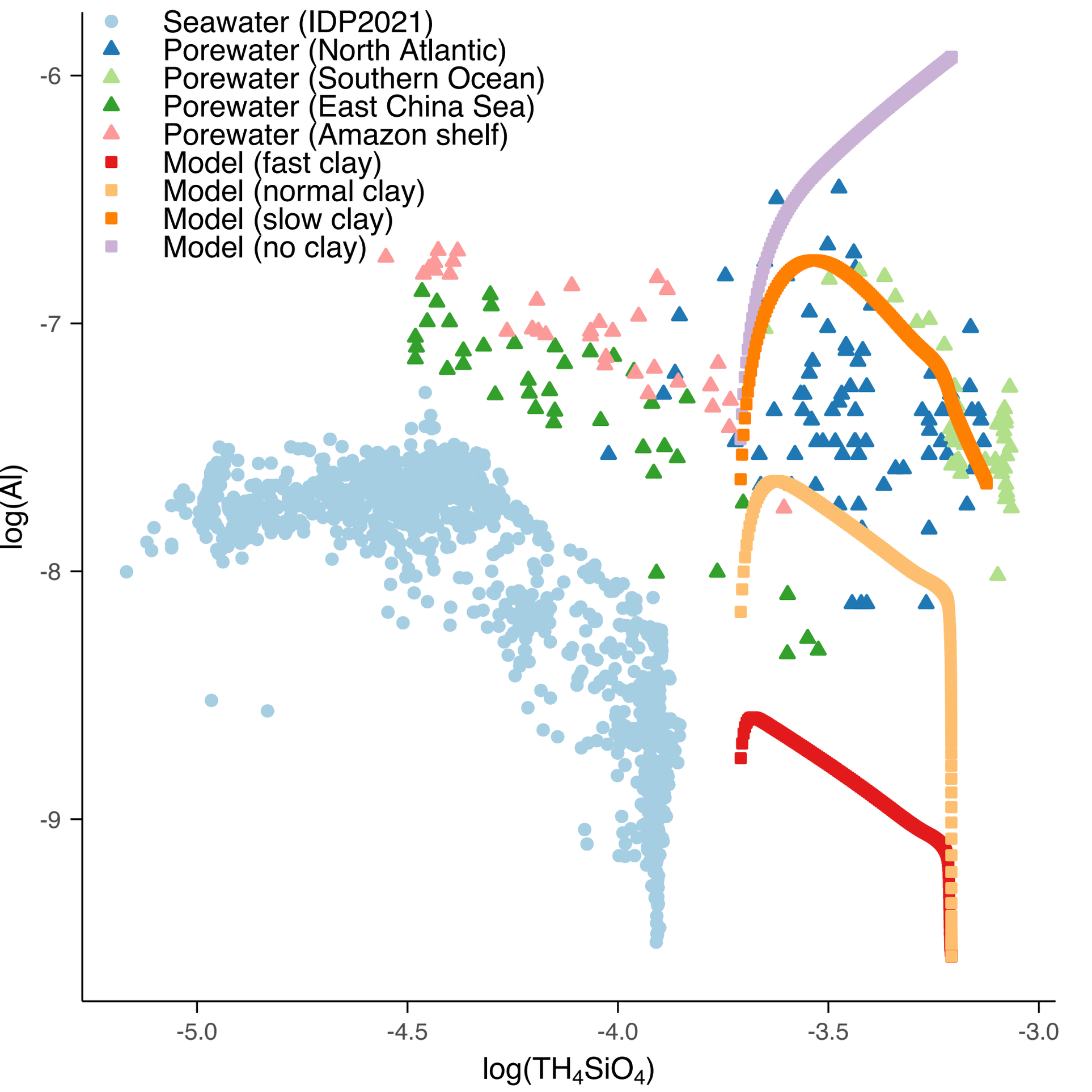
Seawater (IDP2021)
Porewater (North Atlantic)
Porewater (Southern Ocean)
Porewater (East China Sea)
Porewater (Amazon shelf)
Model (fast clay)
Model (normal clay)
Model (slow clay)
Model (no clay)
-6
-7
-8
-9
log(Al)
-5.0
-4.5
-4.0
-3.5
-3.0
log(TH4SiO4)

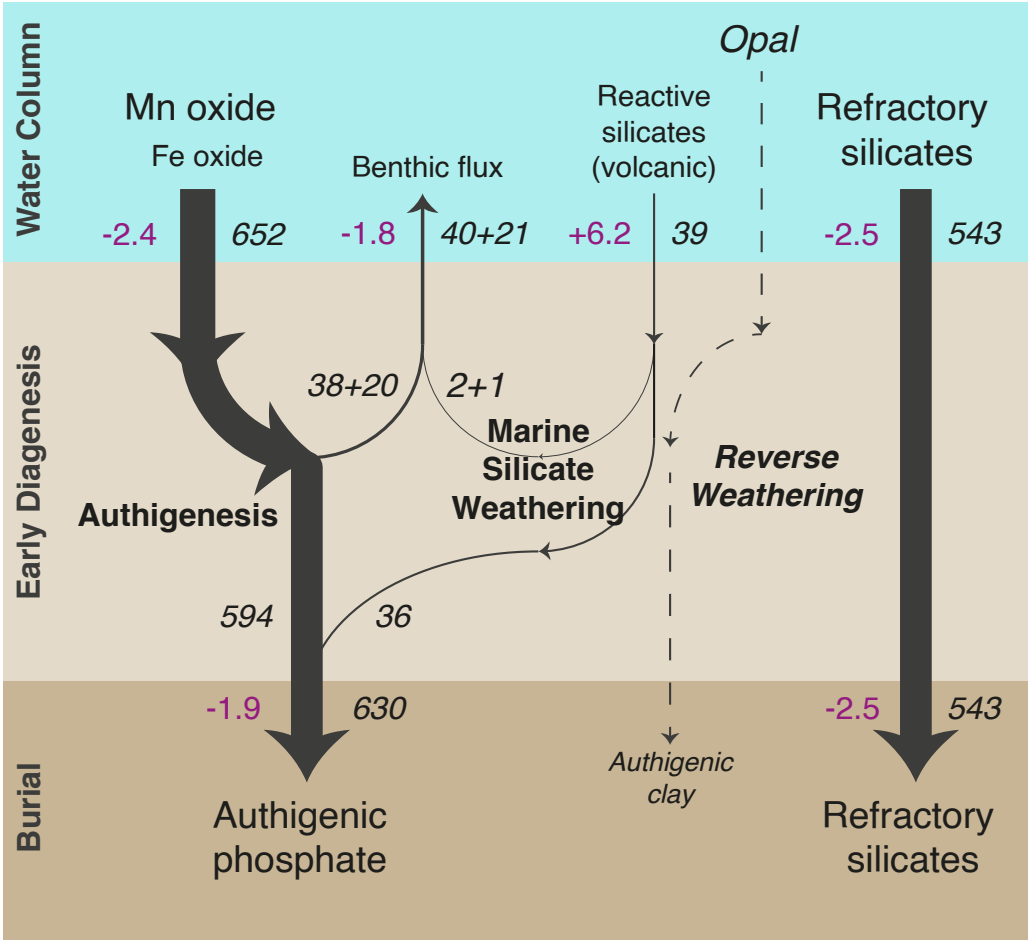
Water Column
Early Diagenesis
Burial
Opal
Mn oxide
Fe oxide
Benthic flux
Reactive silicates (volcanic)
Refractory silicates
-2.4
652
-1.8
40+21
+6.2
39
-2.5
543
38+20
2+1
Marine Silicate Weathering
Reverse Weathering
Authigenesis
594
36
-1.9
630
Authigenic clay
-2.5
543
Authigenic phosphate
Refractory silicates

Supplementary Information

Reactive-transport modeling of neodymium and its radiogenic isotope in deep-sea sediments: the roles of authigenesis, marine silicate weathering and reverse weathering

Jianghui Du[a], Brian A Haley[b], Alan C Mix[b], April Abbott[c], James McManus[d], Derek Vance[a]

[a]Institute of Geochemistry and Petrology, Department of Earth Sciences, ETH Zürich, Clausiusstrasse 25, 8092, Zürich, Switzerland

[b]College of Earth Ocean and Atmospheric Sciences, Oregon State University, 104 CEOAS Admin. Bldg., Corvallis, OR 97331, USA

[c]Department of Marine Science, Coastal Carolina University, 100 Chanticleer Drive E, Conway, SC 29526, USA

[d]Bigelow Laboratory for Ocean Sciences, 60 Bigelow Drive, East Boothbay, ME 04544, USA

Supplementary Methods

1. Diagenetic equations

The concentrations of dissolved (C_d, in mmol/cm^3 pore water) and solid (C_s, in mmol/cm^3 dry sediment) species are modeled using the classic 1-D reactive transport model of early diagenesis (Boudreau, 1997):

$$\varphi \frac{\partial C_d}{\partial z} = \frac{\partial}{\partial z}\left(\varphi D_d \frac{\partial C_d}{\partial z}\right) - \frac{\partial}{\partial z}(\varphi u_d C_d) + \varphi\alpha(C_{BW} - C_d) + \varphi \sum R, \quad (1)$$

$$(1-\varphi) \frac{\partial C_s}{\partial z} = \frac{\partial}{\partial z}\left((1-\varphi) D_s \frac{\partial C_s}{\partial z}\right) - \frac{\partial}{\partial z}((1-\varphi) u_s C_s) + (1-\varphi) \sum R, \quad (2)$$

where φ is porosity, z is sediment depth, C_{BW} is the bottom water concentration and R is the reaction rate. Physical transport includes molecular diffusion corrected for tortuosity (D_d), burial (u_d) and bio-irrigation (α) for dissolved species, and bioturbation (D_s) and burial (u_s) for solid species.

2. Physical transport

The physical transport in the model follows well-established principals in early diagenesis assuming steady state compaction (Berner, 1980; Boudreau, 1997; Dale et al., 2015; Meysman et al., 2003). The parameterizations of the transport terms are reported in Supplementary Table 1 and the parameters are reported in Supplementary Table 2.

3. Biogeochemical reaction network

The biogeochemical reaction network in the model follows the classic studies of early diagenesis including the organic carbon remineralization sequence, secondary redox reactions and minerals such as opal, calcite and Fe sulfides (Berner, 1980; Boudreau, 1997; Dale et al., 2015; Meysman et al., 2003; Wang and Van Cappellen, 1996). The reactions are reported in Supplementary Table 3, the rate expressions are reported in Supplementary Table 4, and the reaction parameters are reported in Supplementary Table 5. Silicate weathering and reverse weathering reactions are reported in Supplementary Table 6.

In the model we use the continuum model of POC reactivity (Boudreau et al., 2008; Boudreau and Ruddick, 1991):

$$k_{POC} = \frac{\nu}{a_0 + a}, \quad (3)$$

Here k_{POC} is the POC remineralization rate, ν controls the shape of the gamma distribution for POC mineralization, a_0 is the initial age of POC, and a is duration of remineralization. We model the deposition age of sediment (Meile and Van Cappellen, 2005) to represent a in Eq. (3):

$$\frac{\partial Age}{\partial z} = \frac{1}{1-\varphi}\frac{\partial}{\partial z}\left((1-\varphi)D_s\frac{\partial Age}{\partial z}\right) - \frac{1}{1-\varphi}\frac{\partial}{\partial z}\left((1-\varphi)u_s Age\right) + 1, \quad (4)$$

4. Adsorption

The adsorption of Nd is described in the main text. In the model, NH_4 adsorption is modeled as (Mackin and Aller, 1984):

$$NH_{4_{ads}} = KNH_{4_{ads}} \times NH_4, \quad (5)$$

Dissolved Fe and Mn can be adsorbed onto FeOOH and MnO_2 (Katsev et al., 2007):

$$Fe_{ads-MnO_2} = KFe_{ads-MnO_2} \times Fe \times MnO_2, \quad (6)$$

$$Fe_{ads-FeOOH} = KFe_{ads-FeOOH} \times Fe \times FeOOH, \quad (7)$$

$$Mn_{ads-MnO_2} = KMn_{ads-MnO_2} \times Mn \times MnO_2, \quad (8)$$

$$Mn_{ads-FeOOH} = KMn_{ads-FeOOH} \times Mn \times FeOOH, \quad (9)$$

5. Aqueous speciation

Speciation reactions and constants are reported in Supplementary Table 7 and 8. To calculate mineral saturation state the model computes pore water pH and the speciation of dissolved Nd, Fe(II) and Al. We follow the Direct Substitution Approach to pH modeling (Hofmann et al., 2008):

$$\frac{\partial H}{\partial t} = \left(\frac{\partial TA}{\partial t} - \frac{\partial TCO_2}{\partial t}\frac{\partial TA}{\partial TCO_2} - \frac{\partial TH_2S}{\partial t}\frac{\partial TA}{\partial TH_2S} - \frac{\partial TB(OH)_3}{\partial t}\frac{\partial TA}{\partial TB(OH)_3}\right) \Big/ \frac{\partial TA}{\partial H}, \quad (10)$$

Proton (H) concentration is modeled dynamically following the impacts of transport and reactions on *total* alkalinity (TA= HCO_3^-+2CO_3^{2-}+ HS^-+ $B(OH)_4^-$+OH^-−H+), total carbon (TCO2= CO_2+HCO_3^-+CO_3^{2-}), total sulfide (TH2S= H_2S+HS^-), total boron ($TB(OH)_3$=$B(OH)_3$+$B(OH)_4^-$) and their individual species. Given modeled pH and assuming local equilibrium, the acid-base equilibria are computed, also including the dissociation of H_4SiO_4 and H_3PO_4, which contribute little to TA but needed for metal speciation. *Apparent* equilibrium constants for seawater are computed at *in situ* temperature (2°C) and pressure

(300 bar) using "seacarb" package (Gattuso et al., 2016) following the best practice recommendation of Dickson et al. (2007).

For Fe(II), complexation with HS^-, CO_3^{2-}, HCO_3^-, Cl^-, SO_4^{2-} are included (Pierrot and Millero, 2017; Rickard, 2006). For Al we consider stepwise hydrolysis (Brown and Ekberg, 2016). *Apparent* equilibrium constants for complex formation and mineral saturation suitable for a seawater medium are either measured, or computed using the constants at zero ionic strength and the activity coefficients from the Pitzer equation based Miami Ion Interaction model of seawater (Pierrot and Millero, 2017). The constants at *in situ* temperature are computed whenever possible, otherwise those at the standard state (25ºC) are used. The pressure effects are generally unknown and thus unaccounted for.

For example, the *apparent* solubility of Nd rhabdophane is computed as

$$\mathrm{Ksp}_{\mathrm{NdPO_4}} = \frac{\mathrm{Ksp}^0_{\mathrm{NdPO_4}}}{\gamma_{Nd^{3+}}\gamma_{PO_4^{3-}}}, \quad (11)$$

where $\mathrm{Ksp}^0_{\mathrm{NdPO_4}}$ is the solubility at zero ionic strength and *in situ* temperature (Gausse et al., 2016), and γ are the activity coefficients in seawater at *in situ* temperature (Pierrot and Millero, 2017).

In the model, pore water concentrations of Cl^-, F^-, Na^+, Mg^{2+}, K^+ are taken to be the same as seawater (salinity=35) as they generally remain constant in surface sediments, while other ligands and species are modeled explicitly. We do not consider organic ligands since they have not been characterized in sediment pore water.

6. Boundary conditions

Boundary conditions of modeled species are reported in Supplementary Table 9. In the model, the flux of Nd is linked to Fe/Mn oxides. In the reversible scavenging formulation, the flux of Nd entering sediments and adsorbed onto MnO_2 (same for FeOOH) is:

$$FNd_{MnO_2-ads} = FMnO_2 \times K_{ads\_MnO_2} \times {}^{i}Nd_{BW}, \quad (12)$$

In the co-precipitation formulation, the flux of Nd entering sediments and co-precipitated with Mn is

$$FNd_{MnO_2-copre} = FMnO_2 \times D_{Nd/Mn} \times \frac{{}^{i}Nd_{BW}}{Mn_{BW}}, \quad (13)$$

Subscript "BW" refers to bottom water and $FMnO_2$ is the flux of MnO_2. Both formulations assume that incoming oxides inherit ε_{Nd} from the bottom water.

Finally, using the modeled pore water Nd concentration, we compute the total benthic Nd flux as the sum of diffusive flux, burial flux and bio-irrigation flux:

$$F_{Nd} = -\phi D_{Nd}\frac{\partial Nd}{\partial z}|_{z=0} + \phi u_d Nd|_{z=0} + \int_{0\ cm}^{50\ cm} \phi\alpha(Nd - Nd_{BW})dz, \quad (14)$$

We compute the benthic flux of both ^{143}Nd and ^{144}Nd, and the ε_{Nd} is computed using the ratio of their fluxes accordingly.

7. Numerical solution

The model code is written in the Julia Language, a programming language for high-performance scientific computing (Bezanson et al., 2017). Diagenetic equations are discretized using the Method-of-Line approach (Boudreau, 1996), resulting in 6600 coupled and stiff ordinary differential equations in the baseline simulation. We solve the sparse system of equations using the CVODE_BDF GMRES solver from the SUNDIALS package (Hindmarsh et al., 2005) included in the Julia package "DifferentialEquations.jl" (Rackauckas and Nie, 2017). The model is run dynamically toward steady state.

8. Data source

Geochemical datasets used in this study are derived from the GEOROC database:
Cascade Arc compilation: https://doi.org/10.25625/PVFZCE/IDBJFS.
Clinopyroxene compilation: https://doi.org/10.25625/SGFTFN/QDDJRA.
Plagioclase compilation: https://doi.org/10.25625/SGFTFN/C8I6RT.

Supplementary Tables

Supplementary Table 1. Parameterization of physical transport

Variables	Parameterization
Porosity	$\varphi(z) = (\varphi_0 - \varphi_L)\exp(-z/z_\varphi) + \varphi_L$
Pore water burial velocity	$u_d(z) = \frac{\varphi_L}{\varphi(z)}\ u_s^L$
Solid sediment burial velocity	$u_s(z) = \frac{1-\varphi_L}{1-\varphi(z)}\ u_s^L$
Final sediment burial velocity	$u_s^L = \frac{F_{sed}}{\rho_s(1-\varphi_L)}$
Bioturbation	$D_s(z) = D_s^0 \mathrm{erfc}(\frac{z-z_s}{2})$
Bio-irrigation	$\alpha(z) = \alpha^0 \exp(-\frac{z}{z_{irr}})$
Molecular diffusion	$D_d(z) = \frac{D_m}{1-\ln(\varphi^2(z))}$

Supplementary Table 2. Parameters of physical transport

Parameter	Explanation	Values	Sources
φ_0	Porosity at 0 cm	0.8	This study
φ_L	Porosity at 50 cm	0.7	This study
z_φ	Porosity attenuation scale	5 cm	This study
F_{sed}	Total sediment flux	1.01×10^{-2} g/cm^2/yr	(Lyle et al., 1992)
ρ_s	Dry sediment density	2.6 g/cm^3	This study
D_s^0	Bioturbation at 0 cm	1.9 cm^2/yr	(Middelburg et al., 1997)
z_s	Mixed layer depth scale	6 cm	(Boudreau, 1994)
α^0	Bio-irrigation at 0 cm	28.4 yr^{-1}	(Meile and Van Cappellen, 2003)
z_{irr}	Irrigation attenuation scale	2 cm	This study
D_m	Molecular diffusivity	Calculated for each species	(Boudreau, 1997)

Supplementary Table 3. Biogeochemical reaction network

Reaction	Explanation	Chemical equation
RO2POC[1]	Aerobic respiration of POC	(CH2O)(NH3)[rNC](H3PO4)[rPC] + O2 + (rNC-rPC)*H{+} = CO2 + rNC*NH4{+} + rPC*H2PO4{-} + H2O
RNO2POC	Denitrification using NO2	(CH2O)(NH3)[rNC](H3PO4)[rPC] + 4/3*NO2{-} + (4/3+rNC - rPC)*H{+} = CO2 + rNC*NH4{+} + rPC*H2PO4{-} + 2/3*N2+ 5/3*H2O
RNO3POC	Denitrification using NO3	(CH2O)(NH3)[rNC](H3PO4)[rPC] + 2*NO3{-} + (rNC - rPC)*H{+} = CO2 + rNC*NH4{+} + rPC*H2PO4{-} + 2*NO2{-} + H2O
RMnO2POC	Mn reduction by POC	(CH2O)(NH3)[rNC](H3PO4)[rPC] + 2*MnO2 + (4 + rNC - rPC)*H{+} = CO2 + rNC*NH4{+} + rPC*H2PO4{-} + 2*Mn{2+} + 3*H2O
RFeOOHPOC	Fe reduction by POC	(CH2O)(NH3)[rNC](H3PO4)[rPC] + 4*FeOOH + (8+rNC - rPC)*H{+} = CO2 + rNC*NH4{+} + rPC*H2PO4{-} + 4*Fe{2+} + 7*H2O
RSO4POC	SO4 reduction by POC	(CH2O)(NH3)[rNC](H3PO4)[rPC] + 1/2*SO4{2-} + (1+rNC - rPC)*H{+} = CO2 + rNC*NH4{+} + rPC*H2PO4{-} + 1/2*H2S + H2O
RCH4POC	Methanogenesis	(CH2O)(NH3)[rNC](H3PO4)[rPC] + (rNC - rPC)*H{+} = 1/2*CO2 + 1/2*CH4 + rNC*NH4{+} + rPC*H2PO4{-}
RO2NO2	Oxidation of NO2 by O2	1/2*O2 + NO2{-} = NO3{-}
RO2NH4	Oxidation of NH4 by O2	3/2*O2 + NH4{+} = NO2{-} + 2*H{+} + H2O
RO2Mn	Oxidation of Mn2+ by O2	1/2*O2 + Mn{2+} + H2O = MnO2 + 2*H{+}
RO2Mn_{ads}[2]	Oxidation of adsorbed Mn by O2	1/2*O2 + Mn_{ads} + H2O = MnO2 + 2*H{+}
RO2Fe	Oxidation of Fe2+ by O2	1/4*O2 + Fe{2+} + 3/2*H2O = FeOOH + 2*H{+}
RO2Fe_{ads}[3]	Oxidation of adsorbed Fe by O2	1/4*O2 + Fe_{ads} + 3/2*H2O = FeOOH + 2*H{+}
RO2H2S	Oxidation of H2S by O2	2*O2 + H2S = SO4{2-} + 2*H{+}
RO2FeS	Oxidation of FeS by O2	9/4*O2 + FeS + 3/2*H2O = FeOOH + SO4{2-} + 2*H{+}
RO2CH4	Oxidation of CH4 by O2	2*O2 + CH4 = CO2 + 2*H2O
RNO2NH4	Anammox	NO2{-} + NH4{+} = N2 + 2*H2O
RSO4CH4	Anaerobic oxidation of methane	SO4{2-} + CH4 + 2*H{+} = CO2 + H2S + 2*H2O
RMnO2Fe	Oxidation of Fe2+ by MnO2	1/2*MnO2 + Fe{2+} + H2O = 1/2*Mn{2+} +FeOOH + H{+}
RMnO2H2S	Oxidation of H2S by MnO2	MnO2 + H2S + 2*H{+} = Mn{2+} + S + 2*H2O
RFeOOHH2S	Oxidation of H2S by FeOOH	2*FeOOH + H2S +4*H{+} = 2*Fe{2+} + S + 4*H2O
RFeSH2S	Precipition of pyrite	FeS + H2S = FeS2 + H2
RFeS_{dis}	FeS dissolution	FeS + H{+} = Fe{2+} + HS{-}
RFeS_{pre}	FeS precipitation	Fe{2+} + HS{-} = FeS+ H{+}
R$CaCO3_{dis}$	Calcite dissolution	CaCO3 = Ca{2+} + CO3{2-}
RBSi_{dis}[4]	Biogenic opal dissolution	SiO2(Al)[rAlSi] + 2*H2O = H4SiO4+rAlSi*Al{3+}

[1]The chemical formula of POC is (CH2O)(NH3)[rNC](H3PO4)[rPC], where *rNC* is the N:C ratio and *rPC* is the P:C ratio.

[2]Mn_{ads} is the sum of Mn adsorbed on MnO2 and FeOOH.

[3]Fe_{ads} is the sume of Fe adsorbed on MnO2 and FeOOH.

[4]Biogenic opal contains Al at an Al:Si molar ratio of *rAlSi*.

Supplementary Table 4. Biogeochemical reaction rates

Reaction	Rate expression
RO2POC	O2/(KO2+O2)*υ/(a0+Age)*POC
RNO2POC	NO2/(KNO2+NO2)*KO2/(KO2+O2)* υ/(a0+Age)*POC
RNO3POC	NO3/(KNO3+NO3)*KNO2/(KNO2+NO2)*KO2/(KO2+O2)* υ/(a0+Age)*POC
RMnO2POC	MnO2/(KMnO2+MnO2)*KNO3/(KNO3+NO3)*KNO2/(KNO2+NO2)*KO2/(KO2+O2)* υ/(a0+Age)*POC
RFeOOHPOC	FeOOH/(KFeOOH+FeOOH)*KMnO2/(KMnO2+MnO2)*KNO3/(KNO3+NO3)*KNO2/(KNO2+NO2)*KO2/(KO2+O2)* υ/(a0+Age)*POC
RSO4POC	SO4/(KSO4+SO4)*KFeOOH/(KFeOOH+FeOOH)*KMnO2/(KMnO2+MnO2)*KNO3/(KNO3+NO3)*KNO2/(KNO2+NO2)*KO2/(KO2+O2)* υ/(a0+Age)*POC
RCH4POC	KSO4/(KSO4+SO4)*KFeOOH/(KFeOOH+FeOOH)*KMnO2/(KMnO2+MnO2)*KNO3/(KNO3+NO3)*KNO2/(KNO2+NO2)*KO2/(KO2+O2)*υ/(a0+Age)*POC
RO2NO2	kO2NO2*O2*NO2
RO2NH4	kO2NH4*O2*NH4
RO2Mn	kO2Mn*O2*Mn
$RO2Mn_{ads}$[1]	kO2Mn_ads*O2*Mn_{ads}*dstopw
RO2Fe	kO2Fe*O2*Fe
$RO2Fe_{ads}$[1]	kO2Fe_ads*O2*Fe_{ads}*dstopw
RO2H2S	kO2H2S*O2*TH2S
RO2FeS	kO2FeS*O2*FeS
RO2CH4	kO2CH4*O2*CH4
RNO2NH4	kNO2NH4*NO2*NH4
RSO4CH4	kAOM*CH4*SO4/(SO4+KAOM)
RMnO2Fe	kMnO2Fe*MnO2*Fe
RMnO2H2S	kMnO2H2S*MnO2*TH2S
RFeOOHH2S	kFeOOHH2S*FeOOH*TH2S
RFeSH2S	kFeSH2S*FeS*TH2S
$RFeS_{dis}$[2]	kFeSdis*FeS*(1-Fe_free*HS/(H*KspFeS)), if Fe_free*HS/(H*KspFeS)<1
$RFeS_{pre}$[2]	kFeSpre*Fe*TH2S*(Fe_free*HS/(H*KspFeS)-1), if Fe_free*HS/(H*KspFeS)>1
$RCaCO3_{dis}$[3]	kCaCO3dis0*CaCO3 + kCaCO3dis1*CaCO3*(1-Ca*CO3/KspCaCO3_dis)^nCaCO3dis, if Ca*CO3/KspCaCO3 <1
$RBSi_{dis}$	kBSi_dis*BSi*(1-TH4SiO4/TH4SiO4_sat), if TH4SiO4/TH4SiO4_sat<1

[1] Rate is converted to unit in per volume of pore water by multiplying $dstopw = (1-\varphi)/\varphi$

[2]Fe_free is the free Fe^{2+} concentration computed using the speciation model.

[3]Calcite dissolution rate is the sum of the close to saturation rate (kCaCO3dis0) and the far from saturation rate (kCaCO3dis1) (Naviaux et al., 2019).

Supplementary Table 5. Biogeochemical reaction parameters

Parameter	Value	Unit[1]	Explanation	Sources
υ	0.125	dimensionless	Shape of the gamma distribution of POC reactivity	(Boudreau et al., 2008)
a0	60	yr	Initial age of POC	This study
rNC	16/117	mol/mol	N:C ratio of POC	(Anderson and Sarmiento, 1994)
rPC	1/170	mol/mol	P:C ratio of POC	This study
KO2	1.00E-06	mmol cm^{-3} pw	Half saturation constant of O2 in POC oxidation	(Dale et al., 2015)
KNO2	1.00E-05	mmol cm^{-3} pw	Half saturation constant of NO2 in POC oxidation	(Dale et al., 2015)
KNO3	1.00E-05	mmol cm^{-3} pw	Half saturation constant of NO3 in POC oxidation	(Dale et al., 2015)
KMnO2	0.03	mmol cm^{-3} ds	Half saturation constant of MnO2 in POC oxidation	(Dale et al., 2015)
KFeOOH	8.8	mmol cm^{-3} ds	Half saturation constant of FeOOH in POC oxidation	This study
KSO4	2.60E-06	mmol cm^{-3} pw	Half saturation constant of SO4 in POC oxidation	(Contreras et al., 2013)
kO2NO2	1.00E+07	(mmol cm^{-3} pw) $^{-1}$ yr^{-1}	Rate of NO2 oxidation by O2	(Dale et al., 2015)
kO2NH4	1.00E+07	(mmol cm^{-3} pw) $^{-1}$ yr^{-1}	Rate of NH4 oxidation by O2	(Dale et al., 2015)
kO2Mn	0.00E+00	(mmol cm^{-3} pw) $^{-1}$ yr^{-1}	Rate of Mn2+ oxidation by O2	(Meysman et al., 2003; Wang and Van Cappellen, 1996)
kO2Mn_ads	1.00E+06	(mmol cm^{-3} pw) $^{-1}$ yr^{-1}	Rate of adsorbed Mn oxidation by O2	(Meysman et al., 2003; Wang and Van Cappellen, 1996)
kO2Fe	1.00E+07	(mmol cm^{-3} pw) $^{-1}$ yr^{-1}	Rate of Fe2+ oxidation by O2	(Meysman et al., 2003; Wang and Van Cappellen, 1996)
kO2Fe_ads	1.00E+06	(mmol cm^{-3} pw) $^{-1}$ yr^{-1}	Rate of adsorbed Fe oxidation by O2	(Meysman et al., 2003; Wang and Van Cappellen, 1996)
kO2H2S	1.00E+05	(mmol cm^{-3} pw) $^{-1}$ yr^{-1}	Rate of H2S oxidation by O2	(Meysman et al., 2003; Wang and Van Cappellen, 1996)
kO2FeS	1.00E+05	(mmol cm^{-3} pw) $^{-1}$ yr^{-1}	Rate of FeS oxidation by O2	(Meysman et al., 2003; Wang and Van Cappellen, 1996)
kO2CH4	1.00E+10	(mmol cm^{-3} pw) $^{-1}$ yr^{-1}	Rate of CH4 oxidation by O2	(Meysman et al., 2003; Wang and Van Cappellen, 1996)
kNO2NH4	1.00E+08	(mmol cm^{-3} pw) $^{-1}$ yr^{-1}	Rate of anammox	(Dale et al., 2015)
kAOM	4.00E-02	yr^{-1}	Rate of anaerobic oxidation of methane (AOM)	(Contreras et al., 2013)
KAOM	1.00E-03	mmol cm^{-3} pw	Half saturation constant of SO4 in AOM	(Contreras et al., 2013)
kMnO2Fe	1.00E+06	(mmol cm^{-3} pw) $^{-1}$ yr^{-1}	Rate of Fe2+ oxidation by MnO2	(Meysman et al., 2003; Wang and Van Cappellen, 1996)
kMnO2H2S	1.00E+04	(mmol cm^{-3} pw) $^{-1}$ yr^{-1}	Rate of H2S oxidation by MnO2	(Meysman et al., 2003; Wang and Van Cappellen, 1996)
kFeOOHH2S	1.00E+01	(mmol cm^{-3} pw)$^{-1}$ yr^{-1}	Rate of H2S oxidation by FeOOH	This study
kFeSH2S	1.00E+07	(mmol cm^{-3} pw) $^{-1}$ yr^{-1}	Rate of pyrite precipitation	(Meysman et al., 2003; Wang and Van Cappellen, 1996)
KspFeS	1.3465E-03	mmol cm^{-3} pw	Solubility of FeS	(Rickard, 2006)
kFeSdis	1.00E-03	yr^{-1}	Rate of FeS dissolution	(Meysman et al., 2003; Wang and Van Cappellen, 1996)
kFeSpre	2.00E+03	(mmol cm^{-3} pw)$^{-1}$ yr^{-1}	Rate of FeS precipitation	This study
kCaCO3dis0	5.54E-02	yr^{-1}	Close to saturation dissolution rate constant of calcite	(Naviaux et al., 2019)
kCaCO3dis1	1.75E+02	yr^{-1}	Far from saturation dissolution rate constant of calcite	(Naviaux et al., 2019)
nCaCO3dis	5	dimensionless	Order of far from saturation dissolution rate of calcite	(Naviaux et al., 2019)
KspCaCO3	7.8636E-07	(mmol cm^{-3} pw)^2	Solubility of calcite	(Gattuso et al., 2016)
kBSi_dis	0.025	yr^{-1}	Dissolution rate of biogenic opal	(Van Cappellen et al., 2002)
TH4SiO4 _sat	6.20E-04	mmol cm^{-3} pw	Saturation concentration of opal dissolution	This study
rAlSi	0.0025	mol/mol	Al/Si ratio in opal	(Van Cappellen et al., 2002)
$KNH4_{ads}$	4.16	cm^3(pw) cm^{-3}(ds)	Adsorption constant of NH4	(Mackin and Aller, 1984)
KMn_{ads_MnO2}	1.00E+04	(mmol cm^{-3} pw)$^{-1}$	Adsorption constant of dissolved Mn on MnO2	(Van Cappellen et al., 2002)
KMn_{ads_FeOOH}	1.00E+02	(mmol cm^{-3} pw)$^{-1}$	Adsorption constant of dissolved Mn on FeOOH	(Van Cappellen et al., 2002)
KFe_{ads_MnO2}	1.00E+04	(mmol cm^{-3} pw)$^{-1}$	Adsorption constant of dissolved Fe on MnO2	(Van Cappellen et al., 2002)
KFe_{ads_FeOOH}	1.00E+04	(mmol cm^{-3} pw)$^{-1}$	Adsorption constant of dissolved Fe on FeOOH	(Van Cappellen et al., 2002)

[1]Units of volume are either referring to pore water (pw) or dry sediments (ds).

Supplementary Table 6. Silicate weathering and reverse weathering reactions.

Reaction	Solubility logK	Rate Logk (mol/m^2/s)	Surface area (m^2/g)[1]	Reference & Comment
Basalt $SiAl_{0.36}O_2(OH)_{1.08} + 0.92H_2O + 1.08H^+ = H_4SiO_4 + 0.36Al^{3+}$	0.64	-8.05	7	(1) Solubility is computed as the stoichiometrically weighted sum of amorphous Si gel and gibbsite dissolution (Gislason and Oelkers, 2003) at *in situ* temperature and pressure using SUPCRTBL (Zimmer et al., 2016). It is then converted to apparent solubility in seawater using the activity coefficient at *in situ* temperature and salinity from the Miami Pitzer Model (Pierrot and Millero, 2017). (2) Dissolution rate at near neutral condition is from (Heřmanská et al., 2022).
Clinopyroxene ($Di_{45}Hed_{25}En_{19}Fs_{11}$) $Ca_{0.7}Mg_{0.84}Fe_{0.46}Si_2O_6 + 4H^+ + 2H_2O = 0.7Ca^{2+} + 0.84Mg^{2+} + 0.46Fe^{2+} + 2H_4SiO_4$	23.63	-11.65	7	(1) Solubility at *in situ* temperature is from (Stefánsson, 2001), then converted to apparent solubility in seawater using the activity coefficient at *in situ* temperature and salinity (Pierrot and Millero, 2017). (2) Dissolution rate at near neutral condition is from (Heřmanská et al., 2022).
Plagioclase ($An_{29}Ab_{71}$) $Ca_{0.29}Na_{0.71}Al_{1.29}Si_{2.71}O_8 + 5.16H^+ + 2.84H_2O = 0.29Ca^{2+} + 0.71Na^+ + 1.29Al^{3+} + 2.71H_4SiO_4$	14.04	-8.41	7	(1) Solubility at *in situ* temperature is from (Stefánsson, 2001), then converted to apparent solubility in seawater using the activity coefficient at *in situ* temperature and salinity (Pierrot and Millero, 2017). (2) Dissolution rate at near neutral condition is from (Heřmanská et al., 2022).
Chlorite $Mg_3Fe_2Al_2Si_3O_{10}(OH)_8 + 16H^+ = 2Fe^{2+} + 3H_4SiO_4 + 2Al^{3+} + 6H_2O + 3Mg^{2+}$	72.92	-13.15	7	(1) Solubility at *in situ* temperature is from the LLNL database (Delany and Lundeen, 1991), then converted to apparent solubility in seawater using the activity coefficient at *in situ* temperature and salinity (Pierrot and Millero, 2017). (2) Dissolution rate at near neutral condition is from (Smith and Carroll, 2016).
Illite $K_{0.85}Al_{2.85}Si_{3.15}O_{10}(OH)_2 + 9.4H^+ + 0.6H_2O = 0.85K^+ + 2.85Al^{3+} + 3.15H_4SiO_4$	18.64	-19.00	55	(1) Solubility at *in situ* temperature is from the Thermochimie database (Marty et al., 2015), then converted to apparent solubility in seawater using the activity coefficient at *in situ* temperature and salinity (Pierrot and Millero, 2017). (2) Precipitation rate is tested in the main text.

[1]Surface areas for primary silicates and authigenic clay are assumed to be 7 and 55 m^2/g respectively following previous studies of marine sediments (Maher et al., 2006).

Supplementary Table 7. Metal speciation

Equation	logK[1]	Sources
Fe{2+} + OH{-} = Fe(OH){+}	3.68	(Pierrot and Millero, 2017)
Fe{2+} + 2*OH{-} = Fe(OH)[2]	5.68	(Pierrot and Millero, 2017)
Fe{2+} + HCO3{-} = FeHCO3{+}	0.58	(Pierrot and Millero, 2017)
Fe{2+} + CO3{2-} = $FeCO3^0$	2.98	(Pierrot and Millero, 2017)
Fe{2+} + 2*CO3{2-} = Fe(CO3)[2]{2-}	4.62	(Pierrot and Millero, 2017)
Fe{2+} + SO4{2-} = $FeSO4^0$	0.82	(Pierrot and Millero, 2017)
Fe{2+} + Cl{-} = FeCl{+}	-0.26	(Pierrot and Millero, 2017)
Fe{2+} + HS{-} = FeS^0 + H{+}	-2.82	(Rickard, 2006)
Al{3+} + H2O = Al(OH){2+} + H{+}	-5.63	(Brown and Ekberg, 2016)
Al{3+} + 2*H2O = Al(OH)[2]{+} + 2*H{+}	-12.74	(Brown and Ekberg, 2016)
Al{3+} + 3*H2O= $Al(OH)[3]^0$ + 3*H{+}	-18.23	(Brown and Ekberg, 2016)
Al{3+} + 4*H2O= Al(OH)[4]{-} + 4*H{+}	-25.85	(Brown and Ekberg, 2016)
Nd{3+} + CO3{2-} = NdCO3{+}	5.46	(Schijf and Byrne, 2021)
Nd{3+} + 2*CO3{2-} = Nd(CO3)[2]{-}	9.56	(Schijf and Byrne, 2021)
Nd{3+} + HCO3{-} = NdHCO3{2+}	0.87	(Schijf and Byrne, 2021)
Nd{3+} + Cl{-} = NdCl{2+}	-0.46	(Schijf and Byrne, 2021)
Nd{3+} + SO4{2-} = NdSO4{+}	1.75	(Schijf and Byrne, 2021)
Nd{3+} + H2O = NdOH{2+} + H{+}	-9.02	(Schijf and Byrne, 2021)
Nd{3+} + H3SiO4{-} = NdH3SiO4{2+}	5.20	(Schijf and Byrne, 2021)
Nd{3+} + 2*H3SiO4{-} = Nd(H3SiO4)[2]{+}	10.80	(Schijf and Byrne, 2021)

[1]Apparent stability constants, either measured at ionic strength of 0.7, or corrected to salinity of 35 using the activity coefficients from (Pierrot and Millero, 2017). We made further corrections to *in situ* temperature (2°C) and pressure (300 bar) whenever possible, otherwise we use the values at the standard state (25°C and 1 bar).

Supplementary Table 8. Acid dissociation

Equation	logK[1]
H4SiO4 = H3SiO4{-} + H{+}	-9.72
H3PO4 = H2PO4{-} + H{+}	-1.59
H2PO4{-} = HPO4{2-} + H{+}	-6.11
HPO4{2-} = PO4{3-} + H{+}	-9.26
CO2 + H2O = HCO3{-} + H{+}	-6.01
HCO3{-} = CO3{2-} + H{+}	-9.32
H2S = HS{-} + H{+}	-6.11
B(OH)3 + H2O + B(OH)4{-} + H{+}	-8.78
H2O = OH{-} + H{+}	-14.13

[1]Computed at *in situ* temperature (2°C), pressure (300 bar) and salinity (35) (Gattuso et al., 2016).

Supplementary Table 9. Boundary conditions[1]

Variable	Type	Value	Unit
POC	Incoming flux	2.7E-3	mmol cm^{-2} yr^{-1}
MnO2	Incoming flux	3.5E-4	mmol cm^{-2} yr^{-1}
FeOOH	Incoming flux	1.1E-4	mmol cm^{-2} yr^{-1}
FeS	Incoming flux	0	mmol cm^{-2} yr^{-1}
FeS2	Incoming flux	0	mmol cm^{-2} yr^{-1}
CaCO3	Incoming flux	1.01E-2	mmol cm^{-2} yr^{-1}
BSi	Incoming flux	3.23E-2	mmol cm^{-2} yr^{-1}
Ca	Bottom water	1.03E-02	mmol cm^{-3}
SO4	Bottom water	2.80E-02	mmol cm^{-3}
TH3BO3	Bottom water	8.71E-05	mmol cm^{-3}
Mn	Bottom water	5.00E-10	mmol cm^{-3}
Fe	Bottom water	5.00E-10	mmol cm^{-3}
Al	Bottom water	5.00E-10	mmol cm^{-3}
CH4	Bottom water	0	mmol cm^{-3}
O2	Bottom water	8.00E-05	mmol cm^{-3}
NO3	Bottom water	4.00E-05	mmol cm^{-3}
NO2	Bottom water	5.00E-08	mmol cm^{-3}
NH4	Bottom water	0.00E+00	mmol cm^{-3}
TH3PO4	Bottom water	2.80E-06	mmol cm^{-3}
TH4SiO4	Bottom water	1.90E-04	mmol cm^{-3}
pH	Bottom water	7.7	free H scale
TCO2	Bottom water	2.38E-03	mmol cm^{-3}
TH2S	Bottom water	0.00E+00	mmol cm^{-3}
Age		0	yr

[1]Boundary conditions at the sediment-water interface. For solid materials, we specify the incoming flux. For dissolved species, we specify the bottom water concentration. Boundary conditions at L=50 cm are no-flux conditions for all species, except for Age, which is $\frac{\partial Age}{\partial z}\big|_{z=L} = 1/u_s^L$.

Supplementary Figures

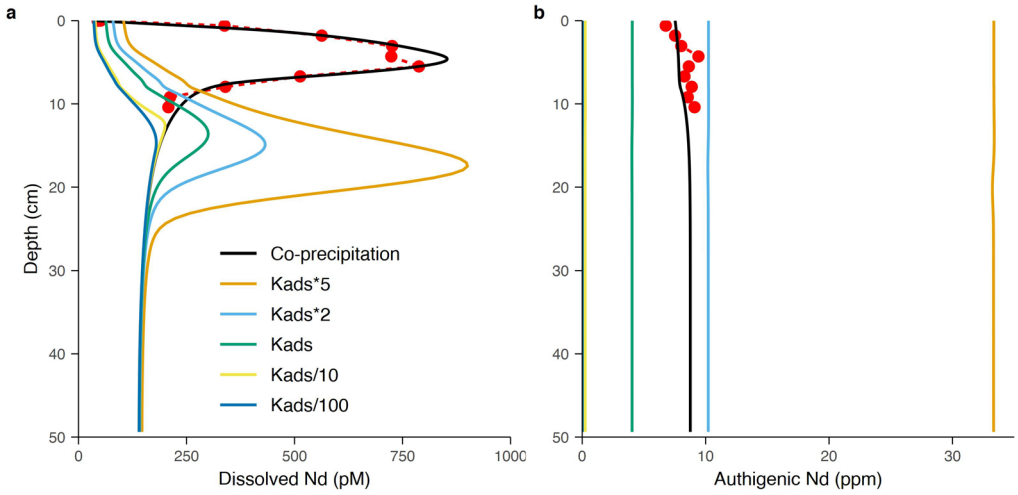

Supplementary Fig. 1. Model sensitivity to adsorption constants in the reversible scavenging formulation of Nd cycling with Fe/Mn oxides. The adsorption constants for both MnO_2 and FeOOH are varied from 5 times ("Kads*5") to 1/100 ("Kads/100") of the values ("Kads") used in the main text in Fig. 4. The results are compared with the co-precipitation formulation and the observations (red dots). The results show that the reversible scavenging formulation cannot capture the depth of the peak dissolved Nd concentration in pore water (**a**). With lower adsorption constants, less Nd is carried by oxides into the sediments, leading to lower pore water (**a**) and authigenic Nd concentrations (**b**).

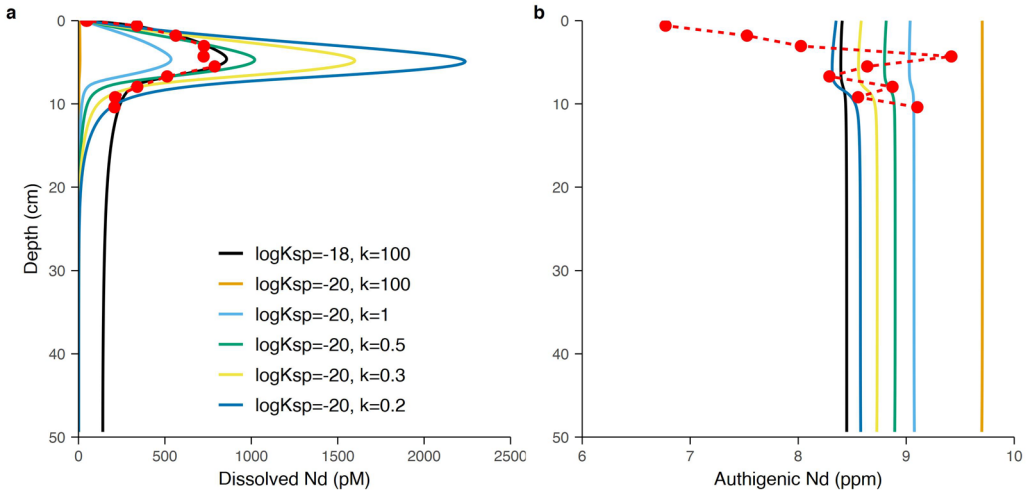

Supplementary Fig. 2. Model sensitivity to the solubility and precipitation rate of $NdPO_4$. The parameters chosen in the main text in Fig. 3 are logKsp= –18 and k=100 pmol/cm^3/yr. In the sensitivity tests we reduce the solubility to logKsp = –20 while decreasing the precipitation rate from 100 to 0.2 pmol/cm^3/yr. With lower solubility, the peak concentration can be captured if reducing the precipitation rate (**a**). However, the resulting peak shapes are narrower than the data suggest. The increase of Nd concentration with depth is delayed close to the sediment water interface, while the decrease of Nd concentration beneath the peak is more abrupt. The best constraint on the parameters would be Nd concentration beneath 20 cm, which would directly reflect the equilibrium concentration with respect to $NdPO_4$, but is unfortunately unavailable. Overall, the fit to the data is worse than using higher solubility (logKsp= –18). Modeled authigenic Nd concentration is not as sensitive considering the data scatter (**b**).

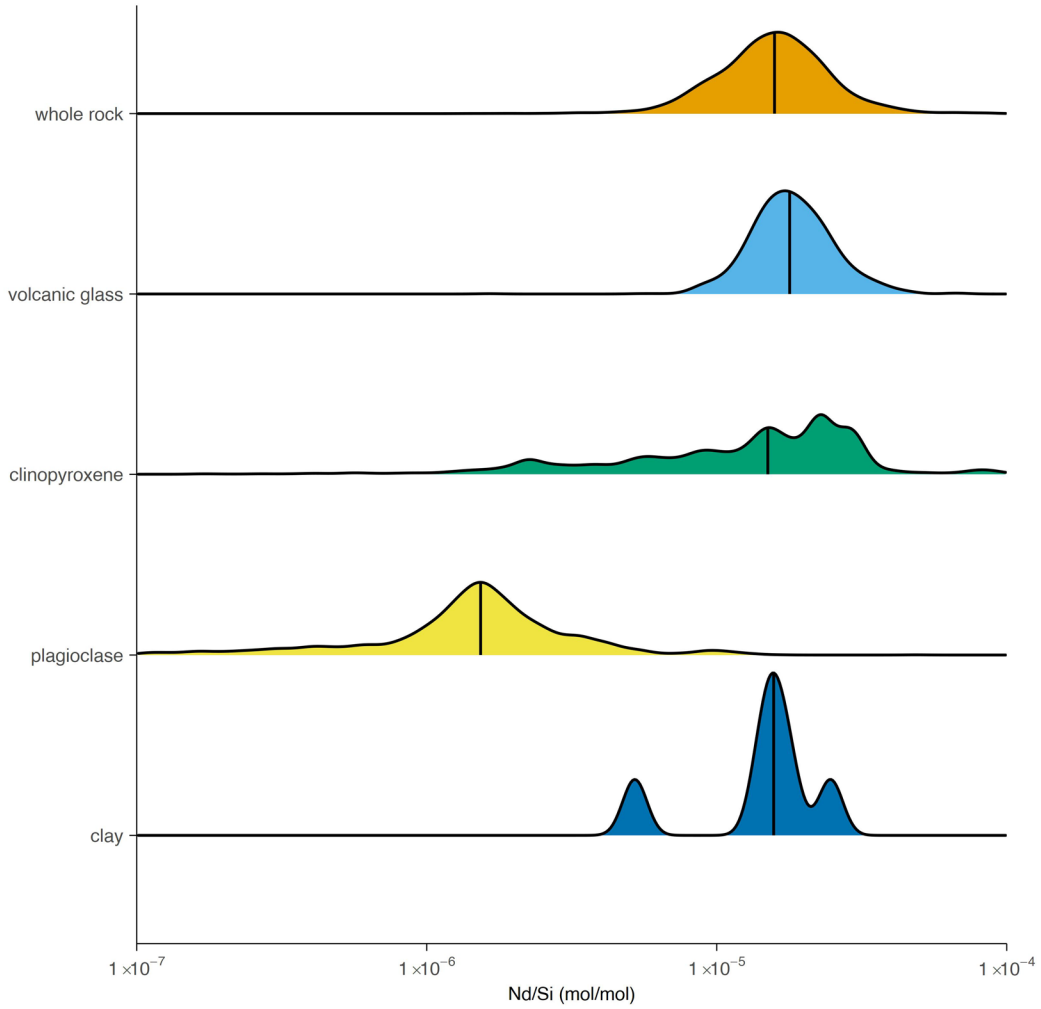

Supplementary Fig. 3. The molar Nd/Si ratio in silicate phases. Data are plotted as probability density graphs (arbitrary y-scale), and the vertical lines indicate median values. Data of whole rock, volcanic glass, clinopyroxene and plagioclase come from the GEOROC database. The whole rock data include all volcanic rock samples from the Cascade Arc. The volcanic glass data are also from the Cascade Arc. The clinopyroxene and plagioclase data are from other convergent margins in the database since no data from the Cascade Arc is found. Clay data are from the global river sediment REE compilation of Bayon et al., (2015), and include the clay data from rivers draining volcanic terrains.

Supplementary References

Anderson, L.A., Sarmiento, J.L., 1994. Redfield ratios of remineralization determined by nutrient data analysis. Global Biogeochemical Cycles 8, 65–80. https://doi.org/10.1029/93GB03318

Bayon, G., Toucanne, S., Skonieczny, C., André, L., Bermell, S., Cheron, S., Dennielou, B., Etoubleau, J., Freslon, N., Gauchery, T., Germain, Y., Jorry, S.J., Ménot, G., Monin, L., Ponzevera, E., Rouget, M.-L., Tachikawa, K., Barrat, J.A., 2015. Rare earth elements and neodymium isotopes in world river sediments revisited. Geochimica et Cosmochimica Acta 170, 17–38. https://doi.org/10.1016/j.gca.2015.08.001

Berner, R.A., 1980. Early Diagenesis: A Theoretical Approach. Princeton University Press.

Bezanson, J., Edelman, A., Karpinski, S., Shah, V., 2017. Julia: A Fresh Approach to Numerical Computing. SIAM Rev. 59, 65–98. https://doi.org/10.1137/141000671

Boudreau, B.P., 1997. Diagenetic models and their implementation : modelling transport and reactions in aquatic sediments. Springer, Berlin; New York.

Boudreau, B.P., 1996. A method-of-lines code for carbon and nutrient diagenesis in aquatic sediments. Computers & Geosciences 22, 479–496. https://doi.org/10.1016/0098-3004(95)00115-8

Boudreau, B.P., 1994. Is burial velocity a master parameter for bioturbation? Geochimica et Cosmochimica Acta 58, 1243–1249. https://doi.org/10.1016/0016-7037(94)90378-6

Boudreau, B.P., Arnosti, C., Jørgensen, B.B., Canfield, D.E., 2008. Comment on "Physical Model for the Decay and Preservation of Marine Organic Carbon." Science 319, 1616–1616. https://doi.org/10.1126/science.1148589

Boudreau, B.P., Ruddick, B.R., 1991. On a reactive continuum representation of organic matter diagenesis. Am J Sci 291, 507–538. https://doi.org/10.2475/ajs.291.5.507

Brown, P.L., Ekberg, C., 2016. Aluminium, gallium, indium and thallium. Wiley VCH, Germany.

Contreras, S., Meister, P., Liu, B., Prieto-Mollar, X., Hinrichs, K.-U., Khalili, A., Ferdelman, T.G., Kuypers, M.M.M., Jørgensen, B.B., 2013. Cyclic 100-ka (glacial-interglacial) migration of subseafloor redox zonation on the Peruvian shelf. PNAS 110, 18098–18103. https://doi.org/10.1073/pnas.1305981110

Dale, A.W., Nickelsen, L., Scholz, F., Hensen, C., Oschlies, A., Wallmann, K., 2015. A revised global estimate of dissolved iron fluxes from marine sediments. Global Biogeochemical Cycles 29, 691–707. https://doi.org/10.1002/2014GB005017

Delany, J.M., Lundeen, S.R., 1991. The LLNL thermochemical data base -- revised data and file format for the EQ3/6 package (No. UCID-21658). Lawrence Livermore National Lab. (LLNL), Livermore, CA (United States).

Dickson, A.G., Sabine, C.L., Christian, J.R., 2007. Guide to best practices for ocean CO2 measurements.

Gattuso, J.-P., Epitalon, J.-M., Lavigne, H., Orr, J., Gentili, B., Hofmann, A., Proye, A., Soetaert, K., Rae, J., 2016. seacarb: Seawater Carbonate Chemistry.

Gausse, C., Szenknect, S., Qin, D.W., Mesbah, A., Clavier, N., Neumeier, S., Bosbach, D., Dacheux, N., 2016. Determination of the Solubility of Rhabdophanes LnPO4·0.667H2O (Ln = La to Dy). European Journal of Inorganic Chemistry 2016, 4615–4630. https://doi.org/10.1002/ejic.201600517

Gislason, S.R., Oelkers, E.H., 2003. Mechanism, rates, and consequences of basaltic glass dissolution: II. An experimental study of the dissolution rates of basaltic glass as a function of pH and temperature. Geochimica et Cosmochimica Acta 67, 3817–3832. https://doi.org/10.1016/S0016-7037(03)00176-5

Heřmanská, M., Voigt, M.J., Marieni, C., Declercq, J., Oelkers, E.H., 2022. A comprehensive and internally consistent mineral dissolution rate database: Part I: Primary silicate minerals and glasses. Chemical Geology 120807. https://doi.org/10.1016/j.chemgeo.2022.120807

Hindmarsh, A.C., Brown, P.N., Grant, K.E., Lee, S.L., Serban, R., Shumaker, D.E., Woodward, C.S., 2005. SUNDIALS: Suite of nonlinear and differential/algebraic equation solvers. ACM Trans. Math. Softw. 31, 363–396. https://doi.org/10.1145/1089014.1089020

Hofmann, A.F., Meysman, F.J.R., Soetaert, K., Middelburg, J.J., 2008. A step-by-step procedure for pH model construction in aquatic systems. Biogeosciences 5, 227–251. https://doi.org/10.5194/bg-5-227-2008

Katsev, S., Chaillou, G., Sundby, B., Mucci, A., 2007. Effects of progressive oxygen depletion on sediment diagenesis and fluxes: A model for the lower St. Lawrence River Estuary. Limnol. Oceanogr. 52, 2555–2568. https://doi.org/10.4319/lo.2007.52.6.2555

Lyle, M., Zahn, R., Prahl, F., Dymond, J., Collier, R., Pisias, N., Suess, E., 1992. Paleoproductivity and carbon burial across the California Current: The multitracers transect, 42°N. Paleoceanography 7, 251–272. https://doi.org/10.1029/92PA00696

Mackin, J.E., Aller, R.C., 1984. Ammonium adsorption in marine sediments1. Limnol. Oceanogr. 29, 250–257. https://doi.org/10.4319/lo.1984.29.2.0250

Maher, K., Steefel, C.I., DePaolo, D.J., Viani, B.E., 2006. The mineral dissolution rate conundrum: Insights from reactive transport modeling of U isotopes and pore fluid chemistry in marine sediments. Geochimica et Cosmochimica Acta 70, 337–363. https://doi.org/10.1016/j.gca.2005.09.001

Marty, N.C.M., Claret, F., Lassin, A., Tremosa, J., Blanc, P., Madé, B., Giffaut, E., Cochepin, B., Tournassat, C., 2015. A database of dissolution and precipitation rates for clay-rocks minerals. Applied Geochemistry, Geochemical Speciation Codes and Databases 55, 108–118. https://doi.org/10.1016/j.apgeochem.2014.10.012

Meile, C., Van Cappellen, P., 2005. Particle age distributions and O2 exposure times: Timescales in bioturbated sediments. Global Biogeochemical Cycles 19. https://doi.org/10.1029/2004GB002371

Meile, C., Van Cappellen, P., 2003. Global estimates of enhanced solute transport in marine sediments. Limnol. Oceanogr. 48, 777–786. https://doi.org/10.4319/lo.2003.48.2.0777

Meysman, F.J.R., Middelburg, J.J., Herman, P.M.J., Heip, C.H.R., 2003. Reactive transport in surface sediments. II. Media: an object-oriented problem-solving environment for early diagenesis. Computers & Geosciences, Reactive Transport Modeling in the Geosciences 29, 301–318. https://doi.org/10.1016/S0098-3004(03)00007-4

Middelburg, J.J., Soetaert, K., Herman, P.M.J., 1997. Empirical relationships for use in global diagenetic models. Deep Sea Research Part I: Oceanographic Research Papers 44, 327–344. https://doi.org/10.1016/S0967-0637(96)00101-X

Naviaux, J.D., Subhas, A.V., Dong, S., Rollins, N.E., Liu, X., Byrne, R.H., Berelson, W.M., Adkins, J.F., 2019. Calcite dissolution rates in seawater: Lab vs. in-situ measurements and inhibition by organic matter. Marine Chemistry 215, 103684. https://doi.org/10.1016/j.marchem.2019.103684

Pierrot, D., Millero, F.J., 2017. The Speciation of Metals in Natural Waters. Aquat Geochem 23, 1–20. https://doi.org/10.1007/s10498-016-9292-4

Rackauckas, C., Nie, Q., 2017. DifferentialEquations.jl – A Performant and Feature-Rich Ecosystem for Solving Differential Equations in Julia. Journal of Open Research Software 5, 15. https://doi.org/10.5334/jors.151

Rickard, D., 2006. The solubility of FeS. Geochimica et Cosmochimica Acta, A Special Issue Dedicated to Robert A. Berner 70, 5779–5789. https://doi.org/10.1016/j.gca.2006.02.029

Schijf, J., Byrne, R.H., 2021. Speciation of yttrium and the rare earth elements in seawater: Review of a 20-year analytical journey. Chemical Geology 584, 120479. https://doi.org/10.1016/j.chemgeo.2021.120479

Smith, M.M., Carroll, S.A., 2016. Chlorite dissolution kinetics at pH 3–10 and temperature to 275 °C. Chemical Geology 421, 55–64. https://doi.org/10.1016/j.chemgeo.2015.11.022

Stefánsson, A., 2001. Dissolution of primary minerals of basalt in natural waters: I. Calculation of mineral solubilities from 0°C to 350°C. Chemical Geology 172, 225–250. https://doi.org/10.1016/S0009-2541(00)00263-1

Van Cappellen, P., Dixit, S., Beusekom, J. van, 2002. Biogenic silica dissolution in the oceans: Reconciling experimental and field-based dissolution rates. Global Biogeochemical Cycles 16, 23-1-23–10. https://doi.org/10.1029/2001GB001431

Wang, Y., Van Cappellen, P., 1996. A multicomponent reactive transport model of early diagenesis: Application to redox cycling in coastal marine sediments. Geochimica et Cosmochimica Acta 60, 2993–3014. https://doi.org/10.1016/0016-7037(96)00140-8

Zimmer, K., Zhang, Y., Lu, P., Chen, Y., Zhang, G., Dalkilic, M., Zhu, C., 2016. SUPCRTBL: A revised and extended thermodynamic dataset and software package of SUPCRT92. Computers & Geosciences 90, 97–111. https://doi.org/10.1016/j.cageo.2016.02.013